10

Melting and Geometric Frustration in Temperature-Sensitive Colloids

Ahmed M. Alsayed, Yilong Han, and Arjun G. Yodh

10.1
Introduction

Colloid science explores the behavior of particles dispersed in a background fluid. Its phenomenology has captured the interest of many scientists across a wide range of disciplines for well over 100 years [1–7]. On the fundamental side, interest in colloids stems from a rich interplay of physical, chemical, and hydrodynamic mechanisms in suspension whose realization provides unique opportunities for the study of statistical mechanics and soft matter. On the more practical side, interest arises as a result of the demonstrated importance of colloids in conventional materials such as paints, motor oils, food, and cosmetics, and in high-tech problems such as photonics [8–16], lithography [17–21], biochemical sensing, and processing [22–40], and in the design of advanced composites [41–49].

Here, we are interested in fundamental science. Over the years, colloidal suspensions have proven to be elegant physical systems for tests of fundamental problems in statistical mechanics ranging from Brownian dynamics [50–77] to entropic phase transformations [78–95]. Their attraction as a model system arises from several factors. Chief among them is that colloids offer well-characterized "thermal" systems whose primary constituents (i.e., particles) can be readily observed and tracked by light scattering techniques or by video microscopy. In this context, colloids are often excellent models for traditional atomic materials with particles playing the role of atoms. In contrast to the atomic systems, however, experimental tools such as laser tweezers [95a], advanced optical microscopy [95b], and the CCD camera are readily used to manipulate particles in suspension [96], to create unusual potentials for the particles [89], and to follow and correlate their particle motions. At present, colloidal particles are used to explore a variety of new classes of interaction and self-assembly phenomenon [78, 97–132] and, more broadly, as a basis for novel measurement technologies [133–140].

The primary unifying feature of the research presented herein is the underlying colloidal system: ensembles of temperature-sensitive microgel particles. In particular, we have used microgel particles to create model lyotropic suspensions whose

phase behavior can be tuned by small variations in temperature rather than by variation in mesogen concentration. The key ingredient in these samples is thermo-sensitive polymer, that is, NIPA polymer (poly(N-isopropylacrylamide)). The tem-perature-sensitive character of our samples stems from the temperature-dependent solubility of NIPA polymer in water. At relatively low temperature, water is a good solvent and NIPA polymer assumes a swollen coil form; in this regime, a small increase in temperature increases monomer–monomer attractions and the size of the isolated polymer coil decreases. Similar ideas apply to NIPA-based microgel particles [141]. In this case, "soft-repulsive" particles made from cross-linked NIPA polymer have diameters that can be tuned by temperature. By changing the particle diameter, one can vary particle volume fraction, and volume fraction is often the primary thermodynamic variable that drives melting and crystallization in colloidal systems [88].

The most significant advantage of these weakly temperature-sensitive suspensions is that changes in temperature enable us to prepare a "lyotropic" colloidal system in particular metastable or ordered states and then to study sample transformations (such as melting) *in situ*. The unique properties of NIPA, in both polymer and microgel particle forms, can therefore be used as a tool to more deeply explore classic physics problems. We have used NIPA *polymer*, for example (see Figure 10.1), to the control liquid crystal transitions of colloidal rods and to study the mechanisms by which lamellar phases melt into nematic phases [142], and we have employed chemically cross-linked NIPA polymer to gels to make new materials, nematic gels with carbon nanotubes, that are analogous to thermotropic liquid crystal elasto-mers [143, 144] (see Figure 10.2).

This chapter will describe recent research on microgel NIPA *particles* rather than NIPA polymer. In contrast to research oriented toward understanding particular chemical and physical phenomenology of NIPA microgel particles and NIPA polymer [145–158], our work takes advantage of the unique properties of microgel particles in order to explore classic physics problems in new ways. In particular, we will describe melting experiments in three-dimensional (3D) colloidal crystals that permit us to investigate the "nucleation" of fluid formation in crystals; these first fluidization events are observed near defects such as grain boundaries [141]. We will also discuss experiments that explore melting of microgel particles in two dimen-sions (2D); this work finds predicted hexatic, fluid, and crystal phases, and it introduces order parameter susceptibility as an experimental means to more clearly define transition points in colloid experiments [159]. Finally, we will describe experiments on geometric frustration [160]. In these measurements, self-assembled colloidal particles on a 2D triangular lattice behave like frustrated antiferromagnetic spins. In contrast to quantum spin systems, however, the NIPA colloidal systems offer the possibility to directly visualize an ensemble of particles (spins), to passively and actively observe their dynamics, and to use temperature to tune "antiferromagnetic" nearest-neighbor interaction strength. Thus, as in the other cases noted above, the microgel colloidal particle approach creates a fresh view of a classic problem. Finally, since our initial submission of this chapter, other recent experiments by us, which utilize the same unique features of NIPA particles, have
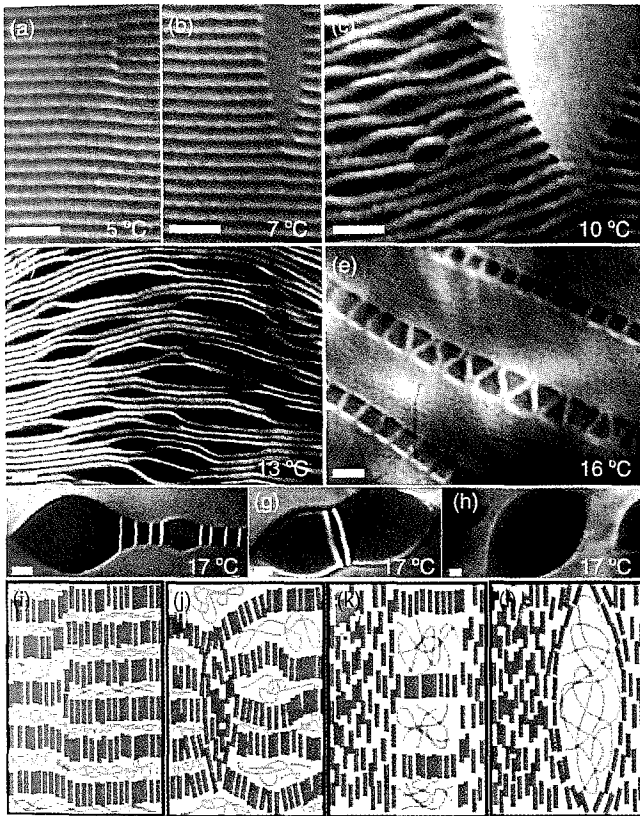
Figure 10.1 Melting behavior of sample of micron-long colloidal rods and NIPA polymers [142]. (a) The lamellar phase at low temperature, consisting of sheets of rods separated by polymer, exhibits visible dislocation defects. (b) At 7 °C, the dislocation defects act as a site for nucleation of the nematic phase. (c) Nematic domains grow, expelling NIPA polymer into lamellar phase, which leads to swelling of lamellar layers. (d) Swollen lamellar phase. (e) Coexistence between nematic phase and highly swollen lamellar phase. (f–g) Isolated monolayer-deformed isotropic tactoid expelling sheets of rods. (h) Isotropic-nematic coexistence observed at high temperature. (i–l) Illustrations of the proposed melting processes of the corresponding rod/polymer mixtures shown in the photographs (a, b, e, h). Scale bars are 5 μm.

proven useful for exploration of the behavior of disordered systems such as glasses [161, 162] and jammed matter [163, 163a], as well as the melting of thin crystalline and polycrystalline films [163b] and freezing criteria in two-dimensions [163c].

The remainder of the chapter is organized as follows. We first introduce the NIPA particle system, providing some discussion of synthesis and characterization. We also describe some of the general experimental and analysis tools that are used. The three sections that follow will describe, respectively, melting in 3D, melting in 2D, and "colloidal antiferromagnets." Finally, the chapter will close with a brief
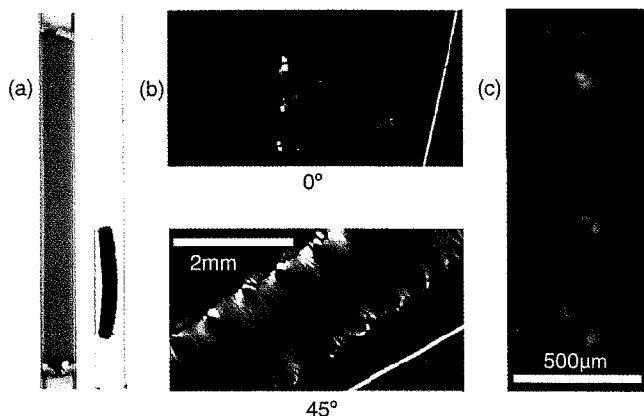
Figure 10.2 Nematic nanotube gel [143] containing isolated half-micron-long single-wall carbon nanotubes (SWNTs). Surfactant-coated SWNTs are homogenously dispersed in a thermally sensitive *N*-isopropylacrylamide gel. SWNT concentration is rapidly increased by shrinking the gel at high temperature. These shrunken gels exhibit hallmark properties of a nematic. (a) Capillary tube containing SWNT-NIPA gels before (left) and after (right) shrinking. (b) Birefringence images of the (shrunken) nematic nanotube gel in different orientations with respect to the input polarizer pass axis. (c) Liquid crystalline defects observed close to the sample edges.

discussion of future directions. Although significant effort will be made to touch on related work, the reader should note that the present chapter is intended to provide a snapshot of the field, rather than a comprehensive review.

10.2
The Experimental System

10.2.1
Synthesis of NIPA Microgel Particles

Poly(*N*-isopropylacrylamide) (NIPA) is a thermally sensitive polymer called PNIPA, PNIPAm, or NIPA, for short. NIPA polymer is known to undergo a coil–globule-type phase transition in water. As temperature is increased, NIPA changes from a predominantly hydrophilic molecule to a predominantly hydrophobic molecule at the lower critical solution temperature (LCST) of ~32 °C [148–155].

Synthesis of microgel particles has been previously reported [145–147, 156]. In our lab, we use the dispersion polymerization technique to synthesize colloidal microgel particles from NIPA polymer.

The simplest scheme to make monodisperse 800-nm diameter NIPA particles (which we did not use for the research reported herein) is to dissolve NIPA monomer and cross-linker monomer (BIS) in water at 78 °C. Then the initiator APS (ammonium persulfate) is added to the solution. In 30 min the particles will grow to their

maximum size. In our case, we employ slightly different procedures so we can attach fluorophores to the particles for microscopy or so we can modify the particle surfaces to have higher surface charges that prevent sticking to glass surfaces.
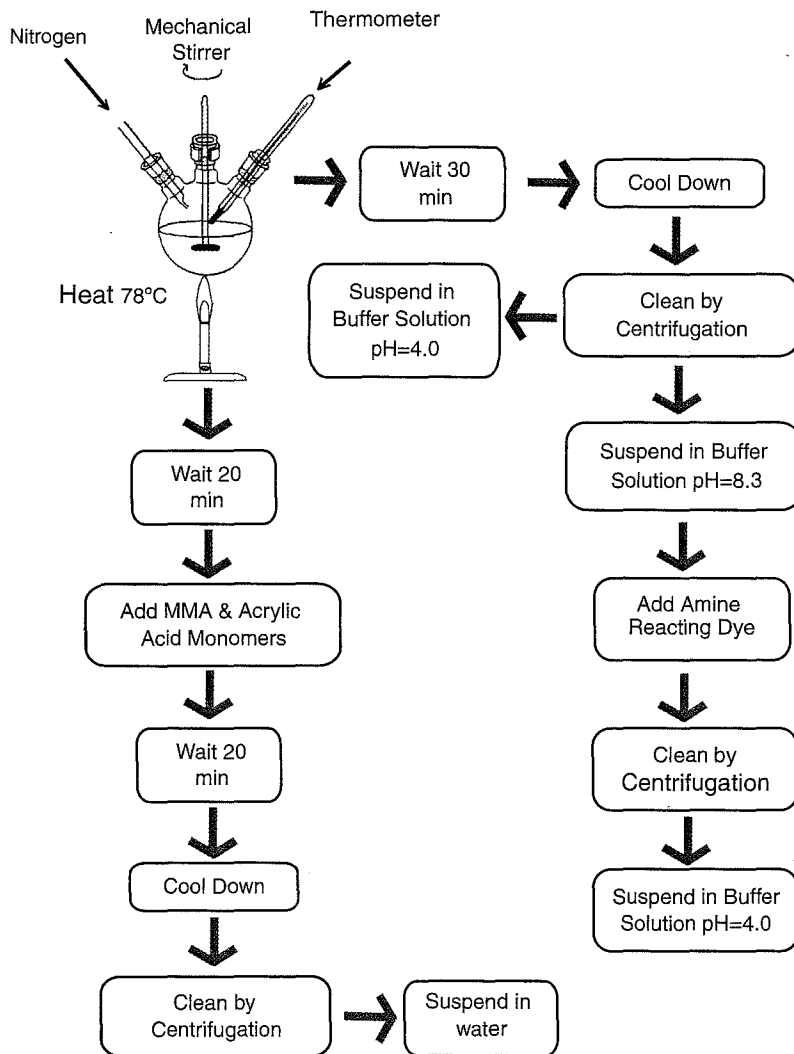
In order to prepare particles with larger negative surface charge, we add MMA (methyl-methacrylate) monomer and acrylic-acid monomer to the solution during the last stage of particle growth, that is, just before the particles reach their maximum size. This procedure effectively renders the surface hydrophilic at all temperatures. Thus, even above the LCST, only the interior of the particle will become hydrophobic.

The procedure employed for the case of added amine-reactive fluorophores is described below. Note, this method will make microgel particles with or without the added fluorophore. The fluorophore we utilize is TAMRA (5-(6)-carboxytetramethylr-hodamine, succinimidyl ester). In this case, the initiator must make the particle surfaces positively charged; the initiator we use is azobis (2,2′-azobis(2-methylpro-pionamidine)). We also increase the number of amine groups per particle by copolymerizing NIPA with 2-aminoethylmethacrylate hydrochloride (AEMA). An AEMA-NIPA copolymer is expected to have higher LCST temperature than pure NIPA ($\sim$32 °C) since AEMA is a hydrophilic monomer. The stability of the beads is also improved by adding a cationic surfactant, didodecyldimethylammonium bro-mide (DTAB) to the suspension. We use BIS (methylene-bis-acrylamide) to cross-link the NIPA polymer within the particles.

The particles are synthesized as follows. First, 20 ml of 25 mM cationic surfactant DTAB, 300 mg of the cross-linker BIS (Polysciences, Inc.), 300 mg of AEMA, 30 gm of NIPA (Polysciences, Inc.), 100 mg of sodium chloride, and 375 ml of 50 mM acetic acid buffer solution, pH = 4.0, are loaded into a special three-neck flask equipped with a stirrer, thermometer, and a gas inlet (see Figure 10.3). The sodium chloride screens the particle surface charges, permitting us to produce bigger particles. In general, particle size can be changed from approximately 800 nm to 2 μm by varying sodium chloride concentration or by initiating NIPA-AEMA copolymerization using APS initiator. The resultant mixture is stirred, heated at 78 °C, and bubbled with dry nitrogen for 10 min to remove dissolved oxygen. (Dissolved oxygen reacts with the initiator, oxidizes the initiator, and it is therefore undesirable.) A solution of 500 mg of 2,2′-azobis(2-methylpropionamidine) dissolved in 10 ml of deionized water is then added to the mixture to start the polymerization reaction. The mixture is continuously stirred at 78 °C for 30 min and then allowed to cool down to room temperature.

The resultant particles are centrifuged and re-suspended in water a few times to remove unreacted monomer, homopolymers, and other salts. The particles are then centrifuged and re-suspended in a buffer solution (pH = 8.3, 0.1 M sodium bicar-bonate) to enable the amine groups to react with the fluorophore TAMRA. Ten milligrams of TAMRA is dissolved in 300 μl of dimethylsulfoxide (DMSO) and then added slowly to 40 ml of particle solution. The solution is gently stirred for 24 h to permit the reaction of the fluorophore to take place.

Finally, the particles are cleaned cyclically, first concentrating them by centrifu-gation and then re-suspending them in a buffer solution (pH = 4.0, 20 mM acetic

Nitrogen　　Mechanical　　Thermometer
　　　　　　Stirrer

Heat 78°C

→ Wait 30 min →　Cool Down

Suspend in Buffer Solution pH=4.0 ← Clean by Centrifugation

Wait 20 min

Add MMA & Acrylic Acid Monomers

Wait 20 min

Cool Down

Clean by Centrifugation → Suspend in water

Suspend in Buffer Solution pH=8.3

Add Amine Reacting Dye

Clean by Centrifugation

Suspend in Buffer Solution pH=4.0

Figure 10.3 Two NIPA particle synthesis schemes, for preparation with negative surface charge (left) and for preparation with added fluorophore (right).

acid). In order to minimize particle aggregates, the suspensions are centrifuged for a few minutes, the supernatant is collected, and the process is repeated (approximately 10 times). For temperatures below 32 °C, NIPA solubility increases with decreasing temperature. Consequently, the NIPA-AEMA particle diameter varies in our experimental temperature regime (20–28 °C) as a result of water moving into and out of the microgel.

A confocal microscopy image of TAMRA-stained NIPA particles is shown in Figure 10.4. Note that particles made of NIPA-AEMA copolymer have higher surface
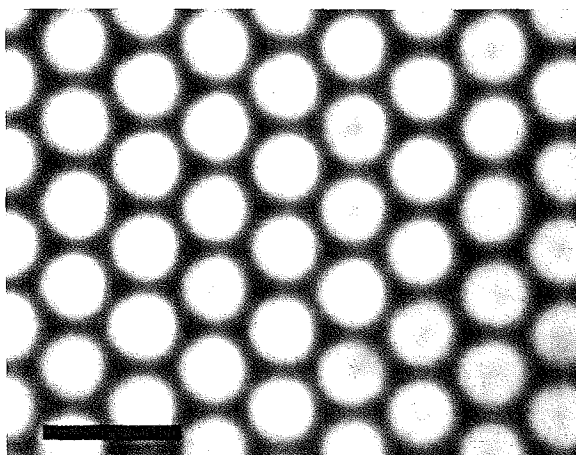
Figure 10.4 Confocal microscopy image of a slice within a NIPA microgel particle colloidal crystal. Scale bar is 3 μm.

charge and are more stable against aggregation in solution *during processing* than particles made of pure NIPA. Counter ions in the buffer solution ensure the charges on the particles are screened. In addition, the polymerization rate in our acidic solutions (pH 4.0) was slow, resulting in reduced size polydispersity. The presence or absence of TAMRA does not appreciably change the particle phase behavior.

10.2.2
Microscopy and Temperature Control

Particle motions were observed by microscope and recorded by CCD camera. In the simplest setup, an analogue CCD camera (Hitachi) is attached to the optical microscope (Leica), and 480×640 pixel images are captured with a video cassette recorder at a rate of 30 images per second. The videotape of particle dynamics is then digitized by a computer equipped with a frame grabber card. Digital images are analyzed to determine the particle positions in each frame (Figure 10.5). For 0.75-μm diameter NIPA spheres, the images are typically obtained with bright field microscopy using a $100\times$ oil objective with numerical aperture equal to 1.45. This gives a magnification of 128 nm/CCD pixel.

In order for particle tracking algorithms to accurately determine particle centers, the number of CCD pixels covered by the image of each particle must be four or more. The colloidal particle position is observed as a circularly symmetric Gaussian image with intensity profile centered about its geometrical center. In general, particle-tracking routines [96] locate particle positions with subpixel accuracy. At a magnification of $100\times$ (8 pixels/μm), subpixel accuracy is obtained, corresponding to spatial resolutions of ~20 nm. Thus, the experimental position resolution for particle tracking in our experiments is approximately one order of magnitude better than
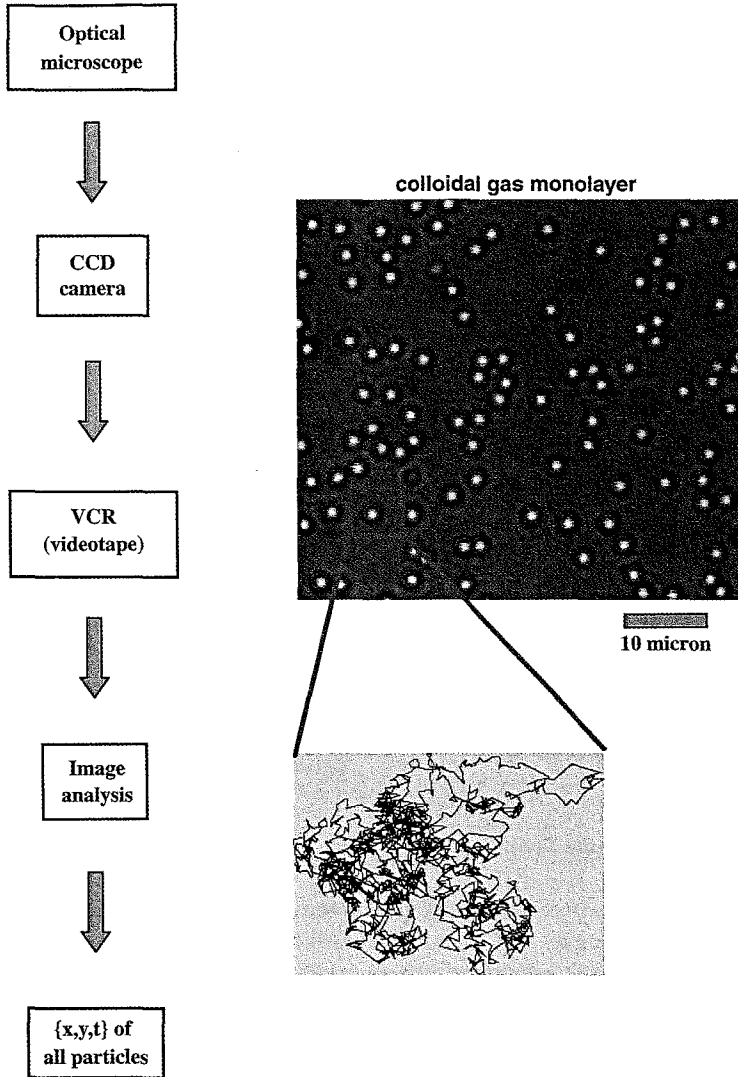
Figure 10.5 Schematic of particle tracking procedure. The image is a colloidal gas monolayer. Overlaid red circles show that the image analysis provides accurate (x,y) positions. The small image is a 1-min trajectory of a particle with 1/30 s per step.

the diffraction limit [96]. The shutter speed of the CCD camera sets an exposure time τ for a single image. If the exposure time is long enough to allow significant particle motion, then the microscope image of the particle will not be circularly symmetric, thus decreasing the ability to assign an accurate particle center. The shutter speed is therefore set so that a particle of radius a embedded in a fluid diffuses less than the spatial resolution, 20 nm, in time τ. The shutter speed in our experiment was
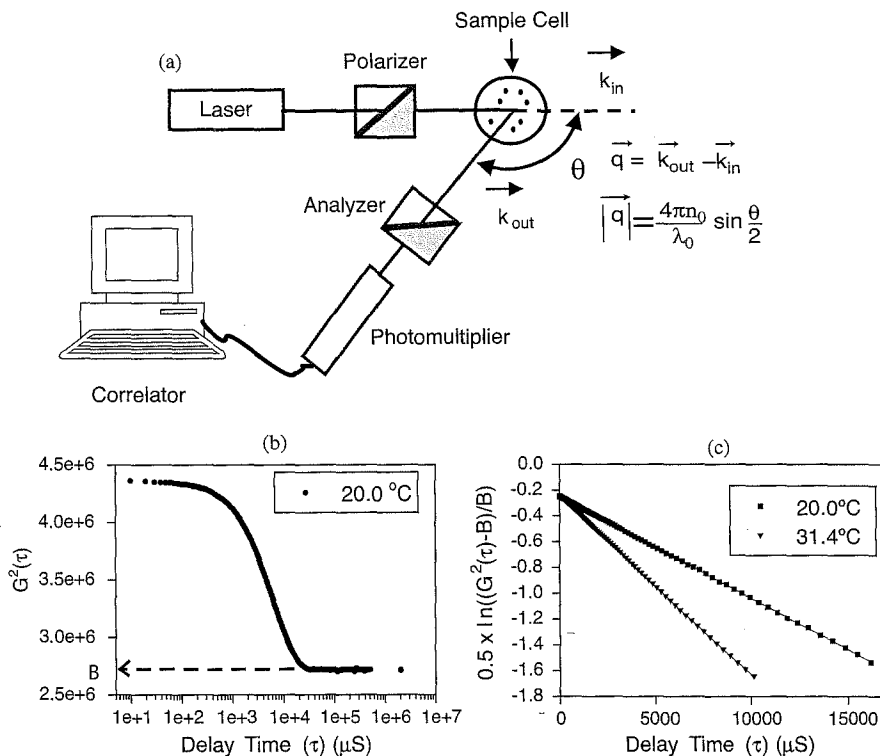
adjusted from 1/500 to 1/2000s. Faster shutter speeds are feasible with our camera, however faster shutter speeds require higher light source intensity. In our experiment, we prefer to lower the light source intensity since too much light absorption can increase the temperature of the sample cell. A spatial "bandpass filter" routine, written by Crocker and Grier [96], was applied to each image to suppress noise and correct for background brightness variations. The particle positions in each frame were obtained using IDL software routines based on intensity weighting determination of the peak position [96].

We use a microscope objective heater to control sample temperature. The temperature control (Bioptechs) has 0.1 °C resolution (Figure 10.6). The small temperature difference ($\sim$0.3 °C) between the objective and the sample has been taken into account in calibration. With this device we were able to heat the sample very slowly, in 0.1 °C/steps; each temperature step typically equilibrated in a few minutes. Measurements were taken after the temperature had stabilized. Before starting the measurements, we cycled the samples one or two times near the melting point in order to relieve any possible shear stress built up during the particle loading process.
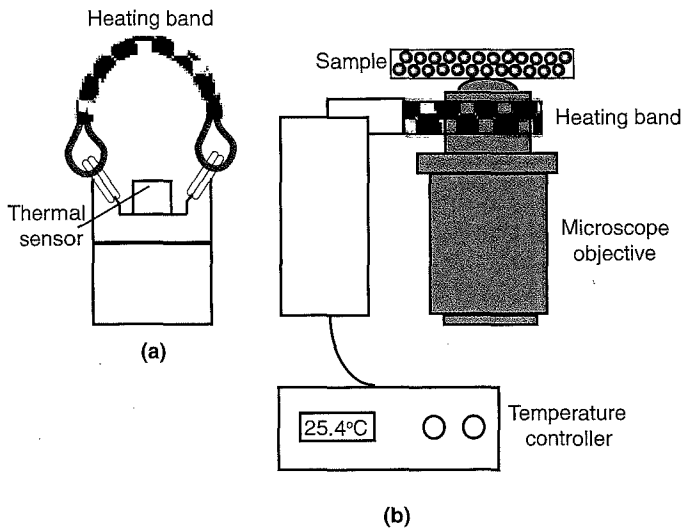
Figure 10.6 Schematic diagram shows microscope objective heating setup. (a) Heater and sensor. The heater is an adjustable thin-film heating band. A surface probe thermal sensor is designed to be in contact with the objective and measures temperature. (b) The objective heater is directly mounted onto the upper region of the microscope objective. The temperature is controlled via electronic temperature controller. This heater/sensor assembly is supported on an adjustable metal mounting to fit over microscope objectives. This configuration can be used on either upright or inverted microscopes.

(a)

Laser — Polarizer — Sample Cell

$\vec{k}_{in}$

Analyzer — $\vec{k}_{out}$

θ $\vec{q} = \vec{k}_{out} - \vec{k}_{in}$

$$|\vec{q}| = \frac{4\pi n_0}{\lambda_0} \sin \frac{\theta}{2}$$

Photomultiplier

Correlator

(b)

$G^2(\tau)$ vs Delay Time (τ) (μS)

20.0 °C

B

4.5e+6, 4.0e+6, 3.5e+6, 3.0e+6, 2.5e+6

1e+1 1e+2 1e+3 1e+4 1e+5 1e+6 1e+7

(c)

$0.5 \times \ln((G^2(\tau)\text{-B})/B)$ vs Delay Time (τ) (μS)

20.0°C
31.4°C

0.0, -0.2, -0.4, -0.6, -0.8, -1.0, -1.2, -1.4, -1.6, -1.8

0   5000   10000   15000

Figure 10.7   (a) Schematic of the dynamic light scattering (DLS) experimental setup. (b) The measured unnormalized intensity autocorrelation function as a function of delay time for a NIPA particle suspension at 20.0 °C. B is the baseline at large τ. (c) Processed data (i.e., electric field autocorrelation functions) at 20.0 and 31.4 °C. Notice that the temporal decay rate is larger at the higher temperature, indicating that the particles have smaller hydrodynamic radii at higher temperature.

10.2.3
Characterization: Dynamic Light Scattering

The hydrodynamic diameter of the microgel particles was measured by dynamic light scattering (DLS) [164, 165]. A schematic of the DLS setup is shown in Figure 10.7. The technique probes the Brownian motion of suspended particles in solution. The particles diffuse in water with diffusion constants that depend on the size of the particles. The light intensity scattered from particles will fluctuate in time as a result of particle diffusion. From the temporal intensity autocorrelation function of the scattered light, one can readily derive useful information about particle diffusion, which, in turn, can be related to particle "average" diameter and sample diameter distribution.

In practice, we measure the (unnormalized) temporal intensity autocorrelation function, $G^{(2)}(\tau) = \langle I(0)I(\tau)\rangle$, and we derive the average particle diffusion coefficient and the particle size distribution from this function. For a monodisperse suspension of particles, the quantity $(G^{(2)}(\tau)-B)/B$ decays exponentially; here, B is the asymptotic value of the intensity autocorrelation function as τ approaches infinity, and the quantity $(G^{(2)}(\tau)-B)/B$ is easily shown to be related to the temporal *electric field* autocorrelation function of the light scattered from the sample. For polydisperse suspensions, a distribution of "diffusion" decay rates will contribute to the autocorrelation signal. The field autocorrelation function will no longer decay purely exponentially. To second-order in the decay time τ, one can show that [164]

$$\frac{1}{2}\ln\left(\frac{G^{(2)}(\tau)-B}{B}\right) = A - \overline{\Gamma}\cdot\tau + \frac{\mu_2}{2}\cdot\tau^2 \tag{10.1}$$

Here, Γ is the "average" exponential decay rate due to particle diffusion, μ_2 is the second-order coefficient of the decay due to particle polydispersity, and A is a constant.

For a dilute particle suspension, Γ depends on the Brownian diffusion of the particles,

$$\Gamma = D\cdot q^2 \tag{10.2}$$

where $|\vec{q}|$ is the absolute value of the experimental momentum transfer, $|\vec{q}| = |\vec{K}_{\text{out}}-\vec{K}_{\text{in}}|$, and D is the average *particle* diffusion coefficient given by Stokes–Einstein relation,

$$D = \frac{k_{\text{B}}T}{6\pi\eta R_{\text{h}}} \tag{10.3}$$

Here, k_{B} is the Boltzmann constant, T is temperature, η is the solvent viscosity, and R_{h} is the average particle hydrodynamic radius.

The particle size and the particle size distribution of our samples is obtained by fitting $0.5\ln\left((G^{(2)}(\tau)-B)/B\right)$ to a polynomial in τ. Then, the average hydrodynamic radius of the particles is obtained from Γ and the polydispersity is obtained from μ_2 (i.e., the variance of Γ). To first approximation, the variance of the hydrodynamic radius distribution is equal to the variance of Γ. This is a good approximation only for narrow particle size distributions, that is, $\Delta R/R \leq 0.30$. By fitting the data obtained from DLS to Equation 10.1, one obtains the polydispersity, P, of the particle hydrodynamic radius, that is,

$$P = \frac{\mu_2}{\overline{\Gamma}^2} \tag{10.4}$$

Figure 10.8 shows the measured hydrodynamic diameter of a sample of microgel particles versus temperature. The DLS analysis shows that sphere polydispersity is lower than 3%. Such small polydispersity is not expected to appreciably affect the colloidal particle melting and crystallization processes [166].

(a)

(b)
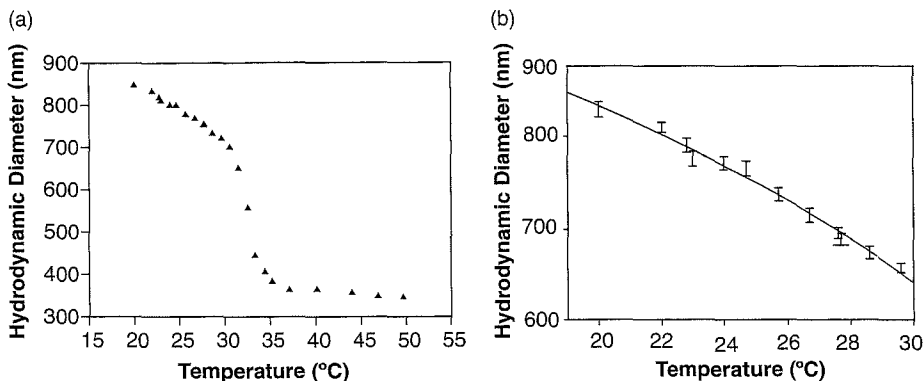
Figure 10.8 (a) Hydrodynamic diameter of NIPA particles as a function of temperature. The NIPA particle hydrodynamic diameter collapses at about 32.0 °C, corresponding to the coil–globule phase transition of the polymer.

(b) A zoom in to the temperature range [20.0–30.0 °C] where the particle volume appears to linearly decrease with temperature (solid line fit).

10.2.4
Characterization: Video Microscopy Measurement of Interparticle Potentials

Particle interactions were derived from direct measurements of their radial distribution function (RDF), $g(r)$. The RDF describes how the density of surrounding particles varies as a function of the distance from a particle center placed at the origin. In a dilute (i.e., areal density $\sim$10%) monolayer of spheres, $g(r = |\mathbf{r}|)$ is the azimuthal average of the pair correlation function

$$\tilde{g}(\mathbf{r}) = \frac{1}{n^2} \langle \varrho(\mathbf{r'} + \mathbf{r})\varrho(\mathbf{r'}) \rangle \tag{10.5}$$

Here, $\varrho(\mathbf{r'}) = \sum_{j=1}^{N(t)} \delta(\mathbf{r} - \mathbf{r}_j(t))$ is the distribution of N particles in the field of view and n is the number density.

In bright field microscopy, though the centers of the individual spheres are characterized by brightness maxima, images will also contain weak alternating dark and bright diffraction fringes. Thus, when two particles are close enough for their fringes to overlap, the apparent (i.e., optically measured) pair separation $\tilde{r}$ deviates systematically from the true particle separation distance r by an amount $\Delta(r)$ [167]. It is important to correct for this effect. To this end, we employed the methods outlined in Ref. [167, 168] to quantify $\Delta(r)$. Briefly, the approach first finds an isolated particle in the colloidal gas monolayer and "cuts" a relatively large subarea around the particle so long as the image clip contains only one sphere. Then, the image clip is duplicated. The image clip and its duplicate are then placed side-by-side at a distance r, and a new "superimposed" intensity image of the "two" particles is thus derived. From the image analysis of this superposed image, we obtained a measured $\tilde{r}$ that
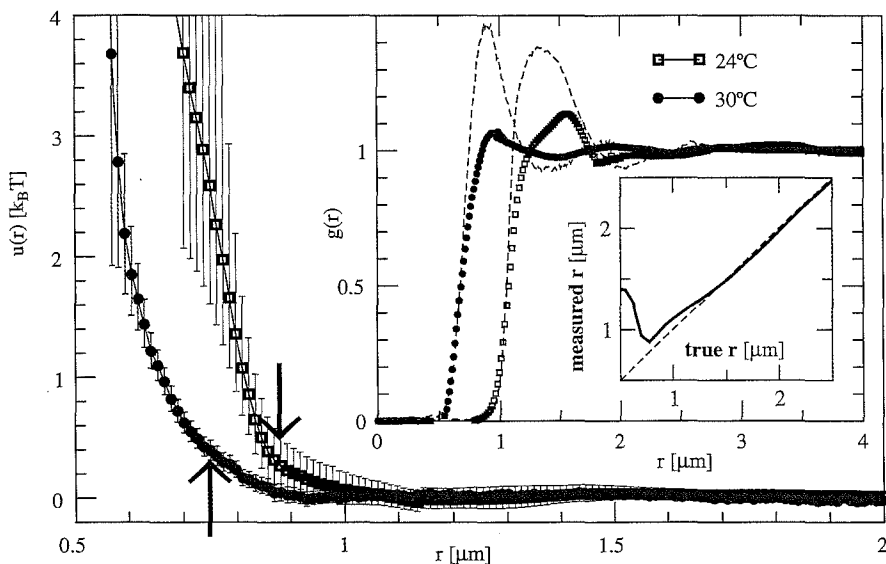
Figure 10.9 The pair potential $u(r)$ of NIPA spheres at 24 °C (square) and 30 °C (circle). Arrows indicate corresponding hydrodynamic diameter measured by dynamic light scattering. *Inset:* The raw $g(r)$ (dashed curve, with the ring artifact) and the corrected $g(r)$ (symbols) without the ring effect. *Small inset:* Measured pair separation with image artifact versus the true separation at 24 °C.

may slightly deviate from the true separation r due to the dark ring surrounded each sphere. We then repeat this process at various distances r, deriving quantitative information about how $\tilde{r}$ changes with r (see the small inset in Figure 10.9). To obtain good statistics, we repeat the above procedure for all isolated spheres in all frames. The undistorted pair correlation function $g(\mathbf{r})$ is then readily related to the directly measured $\tilde{g}(\tilde{\mathbf{r}})$ through conservation of probability [168],

$$g(\mathbf{r})dr = \tilde{g}(\tilde{\mathbf{r}})d\tilde{r} \tag{10.6}$$

As long as the sample's areal particle density is low enough to preclude substantial three-body overlap distortions, one can show that

$$g(\mathbf{r}) = \tilde{g}(\mathbf{r} + \Delta(\mathbf{r}))\left[1 + \frac{d}{dr}\Delta(\mathbf{r})\right] \tag{10.7}$$

where $\Delta(\mathbf{r})$ is the correction to the pair separation (see the large inset of Figure 10.9). Notice that this image artifact is a significant problem in bright field microscopy; its effect is much smaller in dark field microscopy and essentially disappears in fluorescence microscopy (i.e., using fluorescent spheres).

From $g(r)$, we apply liquid structure theory to extract the particle pair potentials [169, 170], $u(r)$, shown in Figure 10.9. We use the following relations [171]:

$$\frac{u(\mathbf{r})}{k_B T} = -\ln g(\mathbf{r}) + \begin{cases} nI & \text{(HNC)} \\ \ln[1 + nI(\mathbf{r})] & \text{(PY)} \end{cases} \qquad (10.8)$$

where n is the mean areal density of the particles.

The first term in the above equation is a Boltzmann relation that is valid for dilute systems where there are no many-body contributions to $g(\mathbf{r})$. For weak many-body contributions, the Boltzmann relation must be corrected. Here, we use the hypernetted chain (HNC) [172] or Percus–Yevick (PY) [172] approximations to correct for many-body effects. $I(r)$ is a convolution integral that can be solved iteratively starting with $I(r) = 0$,

$$I(\mathbf{r}) = \int_A [g(\mathbf{r}') - 1 - nI(\mathbf{r}')][g(|\mathbf{r}' - \mathbf{r}|) - 1]d^2\mathbf{r}' \qquad (10.9)$$

As shown in Figure 10.9, the potentials are short ranged and repulsive, which is consistent with a nearly hard-sphere description [173]. Different batches of microgels have similar $u(r)$. In liquid structure analysis, the HNC approximation is known to be accurate for "soft" potentials while the PY approximation is more accurate for short-ranged hardcore interactions. Here, we observed that both HNC and PY approximations yield almost the same $u(r)$, which suggests good accuracy. We quantitatively estimated other errors, including the statistical uncertainty, errors in image processing, the effects of 3% polydispersity, and the uncertainty stemming from the conversion from $g(r)$ to $u(r)$, which can be estimated as the difference between HNC and PY approximations [170]. The first two error sources dominate. The error bars in Figure 10.9 are total errors. Notice also that the effective particle diameter at $1\,k\,BT$ is ~12% smaller than the hydrodynamic diameter measured by dynamic light scattering (see Figure 10.9). For soft spheres, the diameter is not clearly defined. Here, we use the hydrodynamic diameter R_h for defining the areal or volume fraction, which is the product of the hydrodynamic volume of the individual particle and the areal or volume number density. The areal number density can be measured by optical microscopy, while volume number density requires confocal microscopy.

10.3
"First" Melting in Bulk (3D) Colloidal Crystals

10.3.1
Background

Although melting and freezing are common phenomena in nature, the microscopic mechanisms involved in melting and freezing are still not well understood [174]. Scientists have speculated for more than a century about how crystalline solids melt [174–176], in the process generating microscopic models emphasizing the role of lattice vibrations [177, 178], dislocations [179, 180], grain boundaries [181, 182], surfaces [183–187], dimensionality [188], and combinations thereof.

Furthermore, experimental investigations to test underlying theoretical assumptions are difficult because they must track motions of individual atoms or defects within bulk crystals.

Microgel particle suspensions are especially suitable for the study of phase behavior in 3D. Their refractive index is very close to that of water; thus, both bright field and confocal microscopy can capture the behavior inside the bulk crystal without the detrimental effect of multiple scattering. Furthermore, the microgel particles are very nearly density matched to the solvent (water), so that sedimentation effects will be small. Finally, the microgel particles provide the unique opportunity to tune volume fraction and thus drive the phase transition within a single 3D sample. Compared to conventional colloids, wherein many samples with different particle concentrations must be prepared to study phase transitions, the temperature control characteristic of the NIPA microgel particle suspensions is attractive because it permits us to use one sample for all of the measurements; that is, it permits us to scan a range of volume fractions within essentially the same medium, while visualizing essentially the same sample volume.

A first-principles theory of the solid–liquid transition is not readily available. This theoretical situation contrasts significantly with that of the transitions that arise in ferromagnetism, two-dimensional melting, and liquid–vapor systems. Theoretical issues arise for conventional 3D melting from long-range many-body effects, symmetry, and a lack of universality. Recent experiments [189, 190] and theory [191] have shown that atomic crystal surfaces, at equilibrium below the bulk melting point, often form melted layers. This effect is sometimes referred to as premelting, the localized loss of crystalline order for temperatures below the bulk melting transition. It can be thought of as the nucleation of the melting process. "Premelting" lowers the energy barrier for liquid nucleation and effectively prevents superheating of the solid [189, 192].

Many theories have suggested that a similar "first" melting behavior should occur at defects within bulk crystals such as grain boundaries; however, these effects have not been observed. Simulations of grain boundaries [182, 193–197] have found that the free energy of the solid–solid interface can be larger than two solid–liquid interfaces, thereby favoring "premelting" near the grain boundary (GB). A hot-stage transmission electron microscopy (TEM) experiment [198] has also suggested that GB "premelting" may occur, but only at $0.999T_m$ for pure Al, where T_m is the bulk melting temperature.

In our experiment, we image the motions of particles in three-dimensional crystals during the melting process. These particles are micron-sized nearly hard-spheres [173]. The thermal response of the microgel permits precise control of particle volume fraction. At high volume fraction, these particles are driven entropically to condense into close-packed crystalline solids [88, 199], while at low volume fraction the particles are in the liquid state (see Figure 10.10). Thus by slightly changing sample temperature, we can precisely vary the volume fraction of particles in the crystal over a significant range, driving the crystal from close-packing toward its melting point at lower volume fraction. This general experimental approach enables us to learn about the nucleation of fluid phases inside bulk solids.
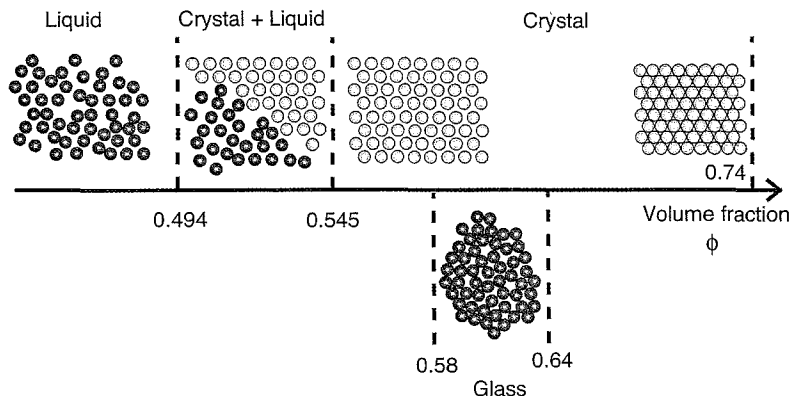
Figure 10.10 Phase behavior of monodisperse hard colloidal spheres.

Experimental images reveal "first" melting near grain boundaries and dislocations. Furthermore, particle tracking enables us to quantify the spatial extent of local particle fluctuations both near a variety of defects and within the more ordered parts of the crystal. Increased disorder and particle fluctuation is observed in regions bordering defects as a function of defect type (e.g., grain boundaries, dislocations, vacancies), distance from the defect, and particle volume fraction. These observations suggest that "first" melting of the grain boundaries is an important effect. Besides their intrinsic importance for colloid science and technology, all indications suggest interfacial free energy is the crucial parameter for melting. Thus, these results are also relevant for atomic-scale materials.

10.3.2
Sample Preparation and Imaging

The particle suspensions were loaded into the chamber using capillary forces at 28 °C, that is, just below the melting temperature. In this process, the suspension was sheared, giving the crystal a preferential orientation. Initially, we found that well-oriented fcc crystals grew from the glass coverslip surfaces and that the middle of the sample was glassy. After loading, we annealed the sample at 28 °C for 24 h during which the samples crystallized. Bragg diffraction (Figure 10.11a) from various parts of the annealed sample, measured using the microscope with a Bertran lens, exhibited no detectable change in peak positions. The colloidal crystal had very few defects close to the glass walls (see Figure 10.11c). We never observed melting near the walls; it is thus possible that the walls stabilized the crystal or that the (1 1 1) planes near the wall surfaces are intrinsically stable [192]. Interior crystalline regions had many more defects (see Figure 10.11d). A few defects in the sample interior are shown in Figures 10.14 and 10.16. Most of the defects observed were stacking faults, which caused the formation of partial dislocations (see Figure 10.16 [200]). Typically, the crystals lost their preferential orientation after melting and recrystallization,
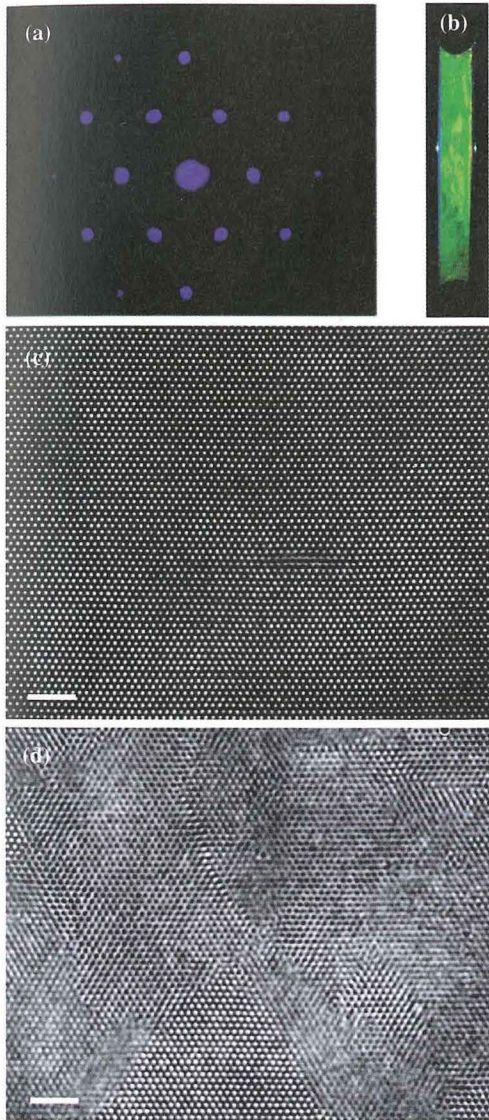
Figure 10.11 (a) Bragg diffraction (wavelength = 405 nm) of 0.75 μm diameter NIPA particle colloidal crystal. (b) Glass chamber containing NIPA particle suspension at high volume fraction. The color indicates that the suspension is in crystalline phase. (c) Bright field image of a layer in the crystal showing very few defects; the slice is of the seventh layer from the cover slip. Each bright spot corresponds to the central region of a 0.75 μm diameter particle. (d) Bright field image of the crystal showing many defects (part of the image is in focus while the other part is out of focus); the slice is of the 15th layer from the cover slip. Due to sample preparation and annealing, the primary defects are partial dislocations that exist in the interior of the crystal. Scale bars are 5 μm.

displaying large crystalline regions with different orientations separated by grain boundaries (Figure 10.14).

Experimental observations were made using an upright microscope (Leica DMRXA2) equipped with a 12-bit monochrome-cooled camera (QImaging RETIGA) and a motorized stage. The dimensions of the sample chamber were $18 \times 4 \times 0.1\,mm^3$. The temperature of the sample and objective lens (100×1.4 NA) was controlled within $0.1\,°C$ and was raised in $0.1\,°C$ increments. Samples were left to equilibrate at each temperature for 1 h. In order to track melted regions and defects, we took bright field video images for 0.6 s in 100 nm intervals throughout the $\sim100\,\mu m$ thick chamber. In order to track individual particle movement, we employed a video shutter time of 2 ms. Image fields were chosen to contain ~400 particles, and particle positions were determined at resolutions much smaller than the particle radius or crystal lattice constant [96]. Fifteen minutes of video were recorded at each temperature. (Note that, although bright-field images can potentially contain image artifacts, we have analyzed these effects [201] and are confident that none of the conclusions we make about the sample is very sensitive to the artifact.)

10.3.3
Positional Fluctuations and the Lindemann Parameter

Using the Lindemann parameter (L), a measure of the particle mean-square fluctuation, we have quantified one aspect of sample melting as a function of sample temperature and volume fraction. Figure 10.12a shows the time evolution of the particle mean square displacement (MSD),

$$\text{MSD}(\tau) = \langle |\vec{r}(t+\tau) - \vec{r}(t)|^2 \rangle \tag{10.10}$$
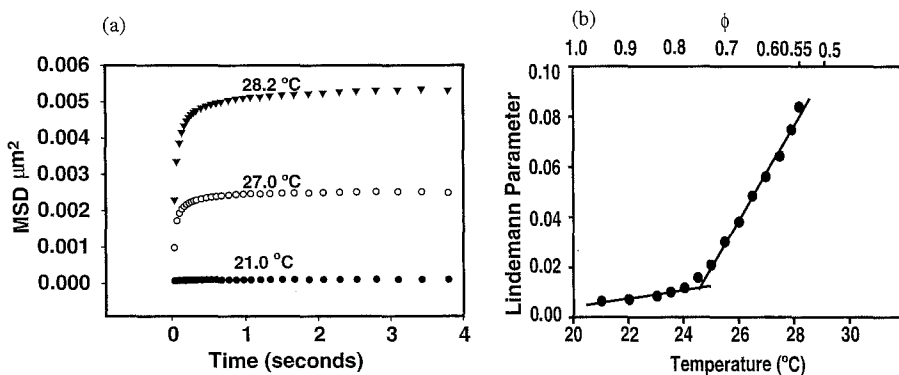
Figure 10.12 (a) Time evolution of 2D particle mean square displacement; L is derived from the MSD plateau value. (b) Lindemann parameter, L, as a function of colloidal crystal temperature (and computed particle volume fraction ϕ). These data are for regions far from defects. The curve exhibits a change in slope at $24.7\,°C$. The crystal melts at $28.3\,°C$, $\phi \sim 0.55$. The error bars for ϕ, L, and temperature are 0.02, 0.004, and $0.1\,°C$, respectively.

for particles in the bulk crystal at three different temperatures, where $\vec{r}(t)$ is the position of the particle center at time t measured from an arbitrary origin (usually the top left corner of the image). On short timescales, the MSD exhibits free particle diffusion; on long timescales, the particles are caged by nearest neighbors and the MSD asymptotically approaches a constant. From this plateau height of MSD measured in a 2D slice, we can calculate 3D Lindemann parameter (L_{3D}):

$$L_{3D} = \frac{1}{r_{nn}} \sqrt{\langle (r_{3D}(\tau \to \infty) - \bar{r}_{3D})^2 \rangle} = \frac{1}{r_{nn}} \sqrt{\frac{3}{2} \langle (r_{2D}(\tau \to \infty) - \bar{r}_{2D})^2 \rangle}$$
$$= \frac{1}{r_{nn}} \sqrt{\frac{3}{4} MSD_{2D}(\tau \to \infty)} \qquad (10.11)$$

where r_{nn} is the lattice constant and $\bar{r}$ is particle's equilibrium position. Here, we assume that particle fluctuations are isotropic so that $MSD_{3D} = \frac{3}{2} MSD_{2D}$. The last step uses the fact that the asymptotic plateau height of MSD is twice the variance of the particle's displacement from its equilibrium position [202, 203].

10.3.4
Bulk Melting

Figure 10.12b shows the measured Lindemann parameter as a function of temperature. The Lindemann parameter experiences a change in slope at 24.7 °C. At this temperature, the hydrodynamic diameter of the particles measured by dynamic light scattering is ~754 nm, and the nearest neighbor distance derived from pair correlation functions measured by microscopy is ~750 nm (Figure 10.13). Thus at this temperature, it is reasonable to assume the particles are close-packed with a volume fraction $\Phi \sim 0.74$. Below this temperature, the particles "press" into one another and
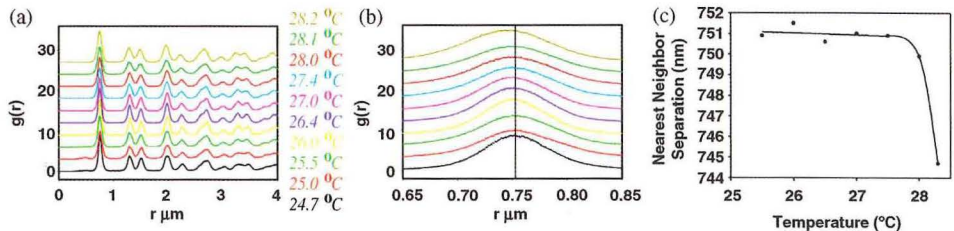
Figure 10.13 Radial distribution function of NIPA crystal at different temperatures. (a) First few peaks of $g(r)$ versus r (b) The first peak of $g(r)$ shows that the lattice constant changes very slightly as the temperature is increased up to the bulk melting temperature. The curves are displaced vertically for clarity. (c) The lattice constant (obtained from the position of the first peak of the pair correlation function) in the solid regions of a NIPA crystal as a function of temperature. Solid line is to guide your eye. Notice that at 28.2 °C the lattice constant starts to substantially decrease; this is approximately the same temperature that wetting appears at partial dislocation interfaces. Note that although the spatial resolution of the measurements is about 20 nm, the 5-nm peak position difference in (c) can still be well resolved if the statistics are good.

the particle motions are constrained; hence, L varies less strongly at low temperature. With this assumption we can deduce the particle number density from $\Phi(T) = n\frac{4}{3}\pi R^3(T)$, where n is the number density and $R(T)$ is particle radius as a function of the temperature (T). Putting $\Phi(24.7\,°C) = 0.74$ and $R(24.7\,°C) = (0.75/2)\,\mu m$ in the above formula, we can deduce particle number density per μm^3. This number density and the measured hydrodynamic radius determine the particle volume fraction (using the above formula), as a function of temperature (upper scale of Figure 10.12b). A particle volume fraction of ~ 0.54 corresponds to a temperature of 28.3 °C. Our *best* samples (i.e., samples with "lowest" disorder) contain very few grain boundaries and noticeably begin to melt at 28.3 °C. Nucleation of melting in these samples is at their center, where the largest concentration of partial dislocations exists. Upon melting, the sample is essentially composed of liquid regions and very ordered (nearly defect-free) crystalline regions. Interestingly, at 28.3 °C the particle volume fraction (based on the assumptions above) is ~ 0.54, close to the hard sphere melting prediction of 0.545 [130].

An alternative approach for establishing bulk melting may be derived from measurements of crystal lattice constant. The lattice constant in the solid regions is derived from our measurements of the particle pair correlation function. It is observed to decrease sharply near 28.3 °C (Figure 10.13c). Again, while our particles are not perfect hard spheres [173], the melting point suggests they may be approximated reasonably well as such.

10.3.5
"First" Melting Near Grain Boundaries

One of the common melting mechanisms exhibited by our colloidal crystals is illustrated in Figure 10.14. In crystals with grain boundaries, the grain boundary interfaces start to disorder at temperatures measurably below 28.3 °C. The figure shows a small angle (i.e., $\sim 13°$) grain boundary. The grain boundary is composed of an array of dislocations, one of which is shown in the inset of Figure 10.14a. Notice that the number of particle nearest neighbors along the grain boundary varies from five to seven (red and blue particles in the inset). These packing mismatches create stress in the crystal near the grain boundary. The dashed line in Figure 10.14a shows a Shockley partial dislocation that continues into the grain boundary. The region to the right (left) of the dashed line is out of focus (in-focus), and the particles in this portion of the image appear darker (whiter) than average.

Figure 10.14b shows the same region at higher temperature (i.e., lower particle volume fraction). In order to minimize the interfacial free energy caused by stress and surface tension, particles near the grain boundary start to melt. The inset of Figure 10.14b shows these particles rapidly jumping from one site to another. In contrast, melting is not observed near the partial dislocation (dashed line); its interfacial free energy is apparently less than that of the grain boundary. In Figure 10.14c, the temperature is slightly higher and melting has erupted along the grain boundary. At this stage, the sample volume fraction is higher than the bulk melting particle volume fraction, and the melted region has engulfed the partial
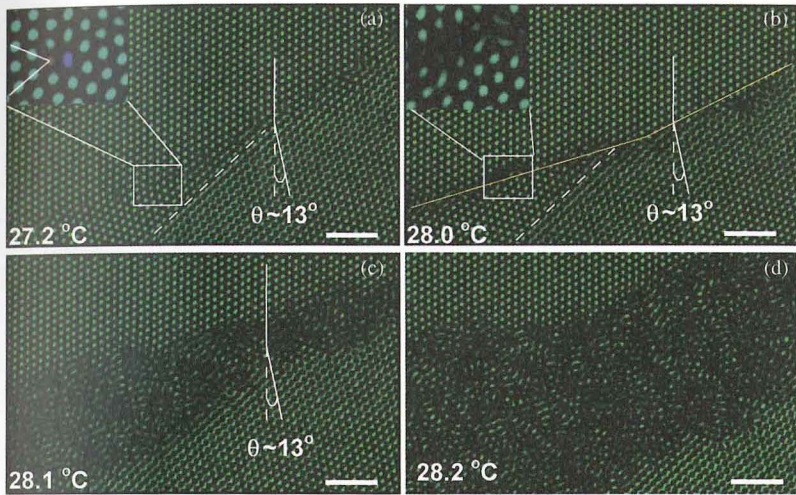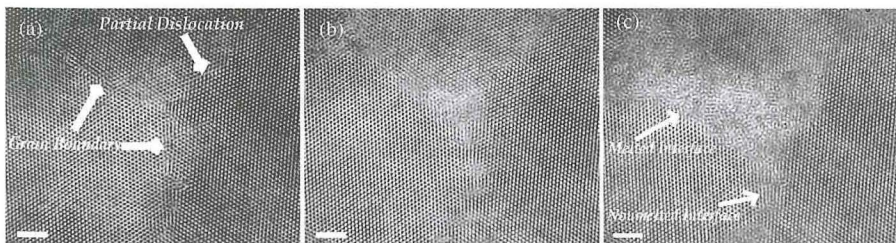
Figure 10.14 Melting of the colloidal crystal at a grain boundary. The figure shows bright field images at different temperatures (i.e., particle volume fractions) of two crystallites separated by a grain boundary ($\theta \sim 13°$). (a) Sample at 27.2°C. The solid and dashed lines show the grain boundary and a partial dislocation, respectively. The grain boundary cuts the two crystals along two different planes (yellow line has two slopes). It is composed of an array of dislocations; the two extra planes are indicated by lines in the inset. (b) Sample at 28.0°C. The grain boundary starts to melt; nearby particles undergo liquid-like diffusion, inset. The partial dislocation, denoted by the dashed line, is not affected. (c and d) The same sample at 28.1 and 28.2°C, respectively. The width of the melt region near the grain boundary increases. Scale bars are 5 μm.

dislocation. The width of the melted region continues to increase as the temperature is raised from 28.0 to 28.2 °C (see Figure 10.14b–d).

Melting is a heterogeneous process, that is, not all interfaces melt at the same temperature. In addition, the number of melted layers depends on the crystalline surface. Figure 10.15a shows a grain boundary that separates two crystallites (right and left). The boundary cuts the two crystallites at two different crystalline surfaces. Each cut has different interfacial energy. Below the bulk melting temperature of

Figure 10.15 (a) Bright field image of a bulk layer in the NIPA particle colloidal crystal showing grain boundaries at 26.4 °C. (b and c) The same layer at 28.2 °C and at 28.3 °C. Scale bars are 5 μm.
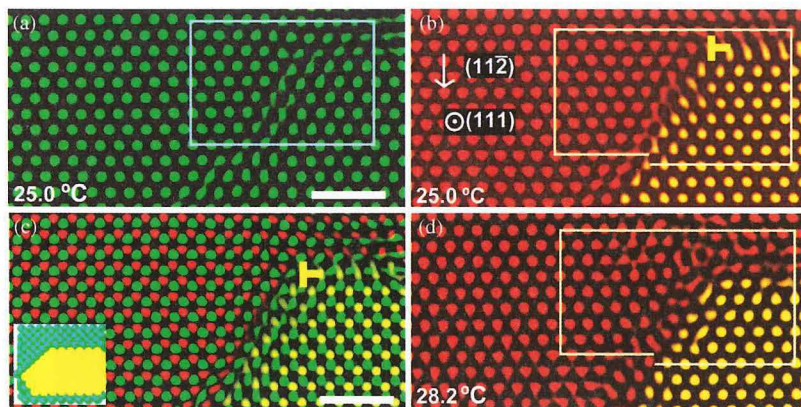
Figure 10.16 Melting of a colloidal crystal initiated at a Shockley partial dislocation in the absence of grain boundaries. (a) and (b) are bright field images of the 61st and 62nd layers at 25.0 °C, respectively. Colloidal particles fluctuate more in the 62nd layer due to the gap created by the dislocation. (c) Superposition of 61st (green) and 62nd (red and yellow) layers. The image shows particles in positions A (green), B (red), and C (yellow). *Inset*, 3D illustration of the 61st–64th layers (bottom to top) showing the displacement of the yellow spheres in the 62nd–64th layers. (d) 62nd layer at 28.2 °C where the crystal starts to melt at the dislocation. Scale bars are 3 μm.

28.3 °C, "first" melting nucleates at certain positions along the grain boundary (see Figure 10.15b). At higher temperatures (lower volume fraction), the number of melted layers increases at the crystalline interface, while remaining unmelted near other interfaces (see Figure 10.15c).

10.3.6
"First" Melting Near Dislocations

In addition to grain boundary melting, the colloidal crystals display melting from partial dislocations (Figure 10.16). This effect is more apparent when the grain boundaries are relatively far from the partial dislocations. Figure 10.16a and b show images of the 61st layer (green) and the 62nd layer (red and yellow) of the colloidal crystal at 25.0 °C, respectively. Figure 10.16c shows a superposition of these layers. Both of these layers represent (1 1 1) planes in the crystal. The Burger's circuit in the 61st layer (green) yields a zero Burger's vector, indicating no defect in the layer. Since a dislocation is present in the next layer, some of the particles are slightly out of focus. The Burger's circuit for the 62nd layer (yellow) reveals a Shockley partial dislocation with a Burger's vector of $\frac{1}{6}(\overline{11}2)$ [200]. The inset contains a three-dimensional illustration of the Shockley dislocation, showing the 61st layer and the undisplaced particles in the 62nd–64th layers in green, and the displaced particles in the 62nd–64th layers in yellow.

In monodisperse nearly hard-sphere colloidal crystals, the difference in energy between face-centered cubic (fcc) and hexagonal close packed (hcp) structures is very

small [204, 205], and stacking faults are very common [88]. Shockley partial disloca-
tions arise as a result of these stacking faults. Face-centered cubic crystals stack in the
pattern ABCABC along the (1 1 1) direction, and hexagonal close-packed crystals
stack in the pattern ABAB. The green particles in Figure 10.16a are in the A positions,
while the red and yellow particles are in the B and C positions of the next layer,
respectively. This stacking fault opens up gaps between the two close-packed
structures within the crystal (two gaps are visible in the image and make an angle
of 120° with respect to one another). Nearby particles fluctuate into and out of these
gaps. The angle the gaps make with the (1 1 1) plane suggest the gaps cut the crystal
along (1 0 0) planes as shown in the three-dimensional illustration. Finally,
Figure 10.16b shows the 62nd crystal layer at 28.2 °C. At this temperature, which
is higher than the grain boundary melting temperature, the crystal has begun to melt
from the partial dislocation.

10.3.7
Positional and Angular Fluctuations Near Defects

The Lindemann melting criterion, which predicts melting for $L \sim 1/8$ [177], con-
tinues to provide a useful benchmark nearly 100 years after it was originally
suggested. The data for L in Figure 10.12b are taken from deep within the crystalline
regions of the sample, below the melting point. At 28.3 °C the sample begins to melt,
and a coexistence of liquid and solid domains is readily observed. In Figure 10.17,
we show local measurements of L near various crystalline defects and near the melt
boundary just before bulk melting (28.3 °C). We find that the particle fluctuations
in the proximity of these regions are measurably larger than in the bulk crystal.
Furthermore, we find the magnitude of these fluctuations to decrease approximately
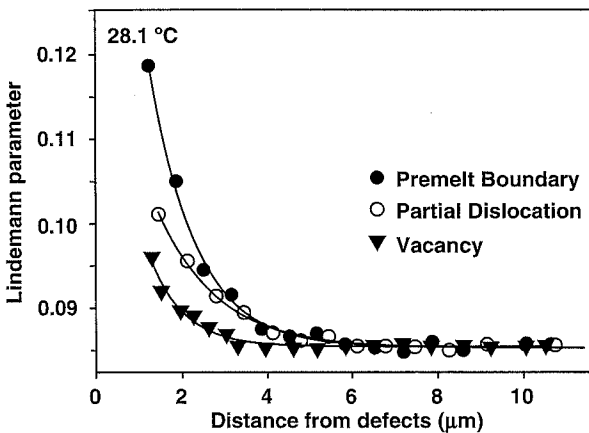

Figure 10.17 The local Lindemann parameter, L, as a function of distance from a vacancy, a partial
dislocation, and a melt front. Within 1 μm of the defects, the particle motion was too rapid and
calculation of L was unreliable.

exponentially as the measurement position is translated away from the melt region toward the interior of the bulk crystal. Extrapolation of our exponential fits of L to zero distance suggest that $L \sim 0.18$ in the melt region, twice its interior value of ~ 0.085 at the same temperature. Evidently, the greater number of vacancies in the melted region increases the free volume for particle movement so that the nearby particle fluctuations are large. Even the particles near isolated vacancies have large L, but the decay length of L to bulk values is shortest from isolated vacancies.

Orientational order is also useful for characterizing different phases in condensed matter systems [206]. For our sample with spherical particles, the orientational order can be measured from the bonds between nearest neighbors via Delaunay triangulation [206, 207]. Delaunay triangulation for a set of points in a plane is a triangulation such that there is no point inside the circumcircle of any triangle. It is the dual graph of the Voronoi diagram. Figure 10.18 shows the Delaunay triangulation near a dislocation.

Notice that instead of viewing the system as a set of vertexes, we can equivalently view it as a set of *bonds* and study the structure and dynamics of these bonds. The static structure of bonds can be quantified by the spatial correlation functions of their orientation [207], which are long ranged in a crystal. Bond dynamics can also be
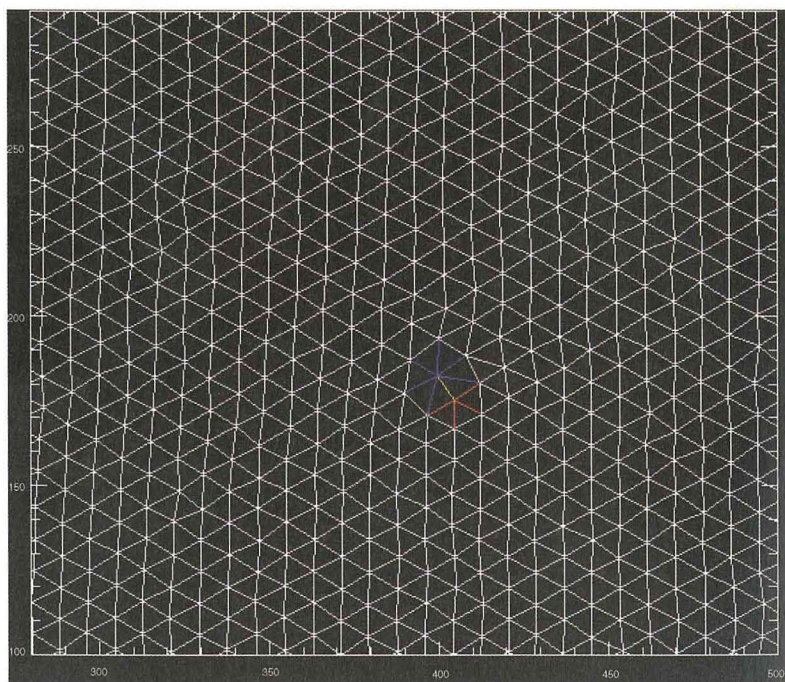
Figure 10.18 Delaunay triangulation of a layer in the bulk colloidal crystal. Colored bonds are associated with defect vortexes with non-six nearest neighbors: white 6–6; blue 7–6; yellow 5–7; red 5–6. Colored bonds show a 5–7 vortex pair, that is, a dislocation.
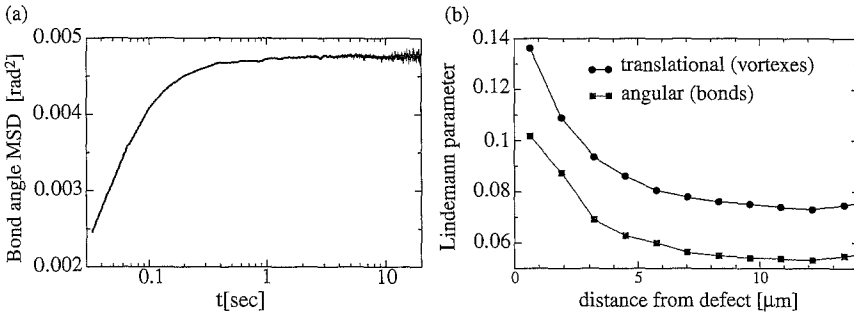
Figure 10.19 (a) Angular MSD of bonds in the crystalline region of Figure 10.18. (b) Translational and angular Lindemann parameters near the dislocation in Figure 10.18. Measurements were taken right before melting temperature. Both quantities decay to crystal values on the same length scale.

characterized by time correlations or bond angle MSDs. Here, we introduce the bond angle MSD, $MSD_\theta(t) = \langle(\theta(t+\tau)-\theta(\tau))^2\rangle$, as a means to characterize bond dynamics. To our knowledge, the notion of bond angle MSD has barely been explored. As in the case of the translational MSD, the angular MSD diverges in the liquid phase and converges to a plateau in crystal phase, see Figure 10.19a.

Neighbor particles are defined from the Delaunay triangulation of the *first video frame* at $\tau = 0$, and we keep tracking the bonds of these neighbor pairs at $\tau > 0$. Thus in the liquid phase, the bond angle of two particles can change by more than 2π after long enough time and yield a diverging angular MSD. Furthermore, we can define an angular Lindemann parameter (L_θ) that is similar to the translational Lindemann parameter in Equation 10.11,

$$L_\theta = \frac{\sqrt{\frac{3}{4}MSD_\theta\,(t \to \infty)}}{\pi/3} \qquad (10.12)$$

where the normalization factor $\pi/3$ is taken from the angle of two neighbor bonds at low temperature in a perfect triangular lattice. Figure 10.19b shows that the angular Lindemann parameter is about 30% lower than the translational Lindemann parameter. Interestingly, both parameters increase in parallel near the defect. Thus, the angular Lindemann parameter can also be used as a criterion for melting and is worthy of further exploration.

10.3.8
Summary

We have demonstrated that "first" melting occurs at grain boundaries and dislocations located within bulk colloidal crystals. The crystals are equilibrium close-packed three-dimensional colloidal structures made from thermally responsive microgel spheres. The thermal response of the microgel enables precision control of particle volume fraction. We used real-time video microscopy to track each particle. Our observations confirm an important mechanism for theories of melting. The amount

of "first" melting depends on the nature of the interfaces and defects. Particle tracking has enabled us to study particle fluctuations both nearby and far from these defects in ways that are inaccessible to experimental probes of atomic crystals, revealing the excess free energy in these regions through higher values of the Lindemann parameter. Our observations suggest interfacial free energy is a crucial parameter for melting, in colloidal and atomic scale crystals.

10.4
Melting in Two Dimensions: The Hexatic Phase

10.4.1
Theoretical Background

Two-dimensional matter is qualitatively different from 3D matter. Questions about the existence of 2D crystals were first raised theoretically in the 1930s by Peierls [208] and Landau [209, 210]. They showed that thermal fluctuations should destroy long-range order, resulting in the melting of any 2D lattice at any finite temperature. Mermin and Wagner further proved that a long-range order in magnetic systems could not exist in both one and two dimensions [211], and they later extended the proof to crystalline order in 2D [212]. However, although true long-range translational order does not exist in 2D, the translational correlations can be quite extended, that is, extended over the finite sample size. In this case, the translational order is said to be quasi-long-range. In addition, 2D systems can have another long-ranged order called *orientational order* [207]. The behaviors of these features distinguish 2D "crystals" from 3D crystals and liquids (see Table 10.1).

The most popular theory for melting in 2D is Kosterlitz, Thouless, Halperin, Nelson, and Young (KTHNY) theory [207, 213–215] that predicts two-stage melting from a 2D crystal to hexatic phase and then from hexatic to liquid phase via two continuous KT transitions (see Figure 10.20). This theory has been confirmed in simulation and experiment for particles with long-range interactions, but is not as

Table 10.1 Translational and orientational orders of different phases.

	Translational order	Orientational order
3D crystal	Long	Long
2D crystal	Quasi-long	Long
Hexatic phase	Short	Quasi-long
Liquid	Short	Short
Buckled 2D crystal	Short	Long

Orders are characterized by correlation functions of the order parameters as shown in Table 10.3. The correlation functions defined in Table 10.2 can have three types of behaviors: approaching a finite constant (long-range order), power law decay (quasi-long-range order), and exponential decay (short-range order).
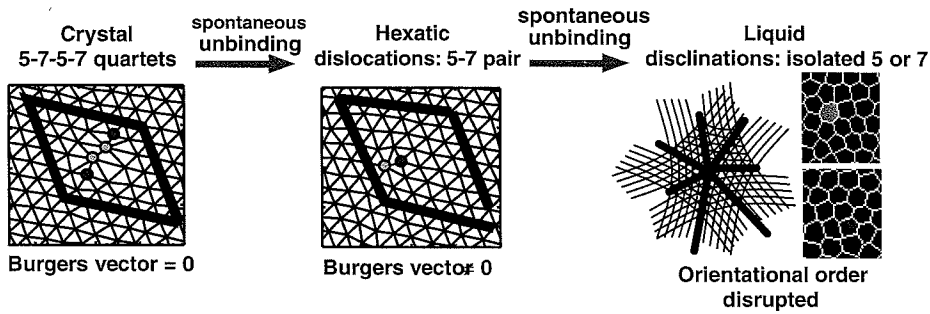
Figure 10.20 Schematic of 2D phases based on KTHNY theory.

well understood in systems with short-range interactions. Here, we study the melting of 2D microgel colloidal crystals confined between two glass walls. KTHNY predictions are thus quantitatively tested in this *short-range* interaction system.

The intermediate hexatic phase of KTHNY theory has short-range translational and quasi-long-range orientational order, and the two transitions from crystal to hexatic phase and then from hexatic to liquid phase are characterized by topological defects, see Figure 10.20. For 2D triangular lattices, nearest neighbors can be characterized by the Delaunay triangulation or its dual structure, the Voronoi diagram. Particles with nearest neighbor $n_n \neq 6$ are considered to be defects. Isolated $n_n = 5$ or 7 defects are called disclinations that can disrupt both translational and orientational order. Isolated 5–7 pairs are dislocations that disrupt the translational order by producing a nonzero Burgers vector, while still preserving the orientational order by keeping the lattice orientation unchanged. KTHNY theory suggests that the creation of free dislocations drives the system from crystal to hexatic phase, and the creation of free disclinations drives the transition from hexatic to liquid phase.

The phases and transitions are characterized by different behaviors of the translational and orientational order parameters. Their fluctuations and correlations are defined in Table 10.2 and its caption. In the local translational order parameter, **G** is the optimal vector that maximizes the order parameter. For crystals, it is simply a reciprocal lattice vector. Usually, **G** is chosen to be a primary reciprocal lattice vector derived from the peak of the structure factor. In the liquid phase, reciprocal lattice vectors are not defined, so we use **G** of the crystal phase to compute ψ_T in the liquid and hexatic phases. This approach has been employed previously [216–218]. To assign accurately **G**, we maximized the sample's translational order parameter ψ_T at each temperature (including the liquid phase), by iteratively varying **G** around the initial estimate.

Orientational order is measured from the "bonds" between nearest-neighbor particles. ψ_{6j}^b in Table 10.2 is a complex local bond orientational order parameter for systems with sixfold symmetry. It is calculated from the position and orientation of the bond j between two nearest-neighbor particles. The triangular crystal's spatial orientational order is reflected by $g_6^b(\mathbf{r}_{jk}) = \langle e^{i6(\theta_j - \theta_k)} \rangle$ between bonds j and k with bond center separation $\mathbf{r}_{jk}$. Alternatively, the local orientational order parameter can

Table 10.2 Translational and orientational order parameters, susceptibilities, and correlations.

	Translational order	Sixfold orientational order
Local order parameter	$\psi_{Tj}(\mathbf{r}) = e^{i\mathbf{G}\cdot\mathbf{r}_j}$	Bond: $\psi_{6j}^b(\mathbf{r}) = e^{i6\theta_j(\mathbf{r})}$
		Particle: $\psi_{6j}(\mathbf{r}) = \left(\sum_{k=1}^{n_n} e^{i6\theta_{jk}}\right)/n_n$
Global order parameter	$\psi_T = |\langle\psi_{Tj}\rangle|$	$\psi_6 = |\langle\psi_{6j}\rangle|$
Susceptibility (fluctuation)	$\chi_T = \lim\limits_{A\to\infty} A(\langle|\psi_T^2|\rangle - \langle|\psi_T|\rangle^2)$	$\chi_6 = \lim\limits_{A\to\infty} A(\langle|\psi_6^2|\rangle - \langle|\psi_6|\rangle^2)$
Spatial correlation	$g_T(r=|\mathbf{r}_i-\mathbf{r}_j|) = \langle\psi_{Ti}^*(r_i)\psi_{Tj}(r_j)\rangle$	$g_6(r=|\mathbf{r}_i-\mathbf{r}_j|) = \langle\psi_{6i}^*(r_i)\psi_{6j}(r_j)\rangle$
Time autocorrelation	$g_T(t) = \langle\psi_{Ti}^*(t_0)\psi_{Ti}(t_0+t)\rangle$	$g_6(t) = \langle\psi_{6i}^*(t_0)\psi_{6i}(t_0+t)\rangle$

G is the optimal vector that maximizes the order parameter. For crystal, **G** is a primary reciprocal lattice vector. Orientational order can be equivalently represented by the particle orientational order parameter ψ_{6j} and by the bond orientational order parameter ψ_{6j}^b. n_n is the number of nearest neighbors of particle j at position $r_j = (x_j, y_j)$; θ_{jk} is the angle of the bond between particle j and its neighbor k; for ψ_{6j}^b, θ_j is the orientation of bond j and $\mathbf{r}$ is the position of the bond center; $\langle\,\rangle$ is the ensemble average over all particles or bonds; A is the system area; and t is the time.

be defined based on particles as shown in Table 10.2. It is simply the average of ψ_{6j}^b over all bonds of particle j. Both ψ_{6j} based on particles and ψ_{6j}^b based on bonds yield the same global order parameter, susceptibility, and correlation functions. We calculated both to double check our data analysis. The global order parameters range from 0 (i.e., totally disordered) to 1 (i.e., perfectly ordered).

The fluctuation of a global order parameter is called its susceptibility χ [219, 220]. For example, χ_T measures the response of the translational order parameter to sinusoidal density fluctuations with periodicity characterized by the primary recip-rocal lattice constant **G**. The divergence or discontinuity of order parameter fluctua-tions, that is, the divergence or discontinuity of its susceptibility, signatures a phase transition. We found that such divergences or discontinuities can be used to determine the phase transition points accurately, avoiding ambiguities inherent to many other analyses. The traditional way to distinguish different phases is from the shapes of the order parameter correlation functions. Correlating single-particle ψ_6 or ψ_T in space or in time yields four correlation functions shown in Table 10.2. The predicted functional forms of these correlation functions in KTHNY theory are listed in Table 10.3. Note, $g_T(r)$ and $g_6(r)$ are two-body quantities, and $g_T(t)$ and $g_6(t)$ are one-body quantities.

Table 10.3 KTHNY predictions for order parameter correlations in three phases.

	Solid	Hexatic	Liquid
$g_6(r)$	Nonzero constant at $r\to\infty$	$\sim r^{-\eta_{6r}}$, $0 < \eta_{6r} \leq 1/4$	$\sim e^{-r/\xi_{6r}}$
$g_6(t)$	Nonzero constant at $t\to\infty$	$\sim r^{-\eta_{6t}}$, $0 < \eta_{6t} = \eta_{6r}/2 \leq 1/8$	$\sim e^{-t/\tau}$
$g_T(r)$	$\sim r^{-\eta_{Tr}}$, $1/4 < \eta_{Tr} \leq 1/3$	$\sim e^{-r/\xi_{Tr}}$	$\sim e^{-r/\xi_{Tr}}$

10.4.2
Experimental Background

Experimenters have sought out KTHNY predictions across a wide range of materials including monolayers of molecules and electrons [221], liquid crystals [222], vortex lattices in superconductors [223], diblock copolymers [224], and colloidal suspensions [225–231]. Compared to other materials, colloids have the advantage of measurable single-particle dynamics in real space. Some experiments and simulations have demonstrated substantial agreement with KTHNY theory, but others exhibit deviations and ambiguities possibly due to finite size effects [221], interaction range and form [227], and out-of-plane fluctuations [216, 220]. Charged colloids with screened Coulomb repulsion were the first colloidal systems used in the search for the hexatic phase. In these experiments [225, 232, 233], charge stabilized colloidal suspensions are filled in chambers with two smooth glass walls. The two glass walls form a wedge with a small angle. The spheres repel each other and are repelled by the glass plates due to surface charges, so that squeezing the plates closer together lowers the areal density of the spheres in between. Thus, the gradual change in plate separation induces gradual density gradient along the wedge. This system exhibited the hexatic phase, but the topological defects found in the system were complex and were not consistent with the simple KTHNY picture [225]. Nearly hard spheres with very short-range *attraction* [226] have been studied in a series of samples with different packing fractions; in this case, two first-order transitions and a middle hexatic phase were reported [226]. However, similar colloids with purely short-range *repulsion* did not exhibit a hexatic phase during melting [227]. Arguably the most well defined system to investigate the hexatic phase are monolayers of magnetic spheres with long-range (tunable) dipole repulsion [228, 229]. Many KTHNY predictions have been confirmed within this system class including the structural properties [228], the dynamics [229], and the crystal's elasticity [230]. Thus, the preponderance of simulation and experimental evidence clearly points to the validity of the KTHNY scenario in 2D systems with long-range interaction potentials [228–230, 234]. The evidence is less convincing, however, in systems with *short-range interactions* [219, 235–238a]. Note that KTHNY theory does not guarantee a scenario with a middle hexatic phase, and different 2D systems may have different melting paths as shown in the phase diagrams of Figure 2.21 in Ref. [207].

The NIPA microgel particles are ideal to study 2D melting. The pair potential between particles is short ranged and repulsive, and temperature tuning can be used to vary sample volume fraction and drive the melting transition. Furthermore, temperature-sensitive particles enable us to follow the spatiotemporal evolution of the *same* sample area through the entire sequence of transitions. This feature is attractive and was not realized in previous colloidal samples that employed charged spheres in the wedge geometry with density gradients [225] or in the more hard-sphere-like systems that employ a series of concentration-dependent sample cells [226]. In the wedge geometry, different densities are achieved at different wall separations that can affect correlations and the phase behavior. The same problem exists when making a series of samples; the samples are hard to make uniformly and

it is also difficult to accurately measure and control wall separations in different cells [226]. Finally, the nontunable systems are more easily trapped in metastable glassy states [226]. By contrast, our temperature-sensitive samples start in the equilibrium 2D crystal phase and re-equilibrate rapidly after each tiny (0.2 °C) temperature step. They are, therefore, far less likely to be trapped in metastable glassy states during melting. Again, although the recent experiments using magnetic spheres with tunable dipole–dipole interactions [228–230] share some of these advantages, they also differ from the microgel experiments in a complementary way as a result of their *long-range* dipolar interactions.

10.4.3
2D Samples

Samples consisted of a monolayer of NIPA spheres confined between two glass coverslips (see Figure 10.21). Dynamic light scattering measurements found the NIPA sphere hydrodynamic diameter to vary from 950 nm at 20 °C to 740 nm at 30 °C. Note that we conducted this experiment with larger NIPA particles than the particles that are used in the 3D melting experiment (see Figure 10.8); however, the behavior of both samples is similar as a function of temperature. The cleaned glass surfaces were coated with a layer of 100 nm diameter NIPA spheres to prevent particle sticking. A simple geometric calculation showed that 100 nm close-packed spheres on the surface give rise to 3 nm surface roughness for the 800 nm diameter spheres. This surface roughness is negligible compared to sphere polydispersity and wall separation fluctuations. In addition, our observations of the large sphere motions at lower concentrations did not find evidence for preferential spatial locations, that is, significant surface potentials. We increased the temperature from 26.5 to 28.5 °C in 0.2 °C steps and recorded 5 min of video at each temperature.
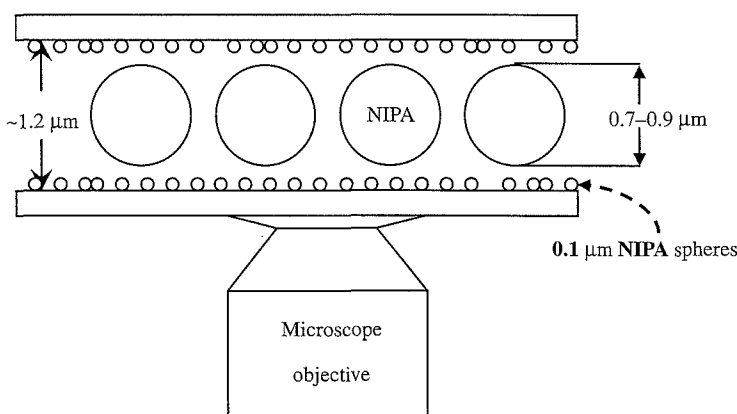
Figure 10.21 Schematic of 2D sample cell. A uniform layer of 0.1 μm diameter NIPA spheres is coated on the inner surfaces in order to avoid large NIPA particles sticking on glass walls. (The microscope objective is not drawn to scale.)
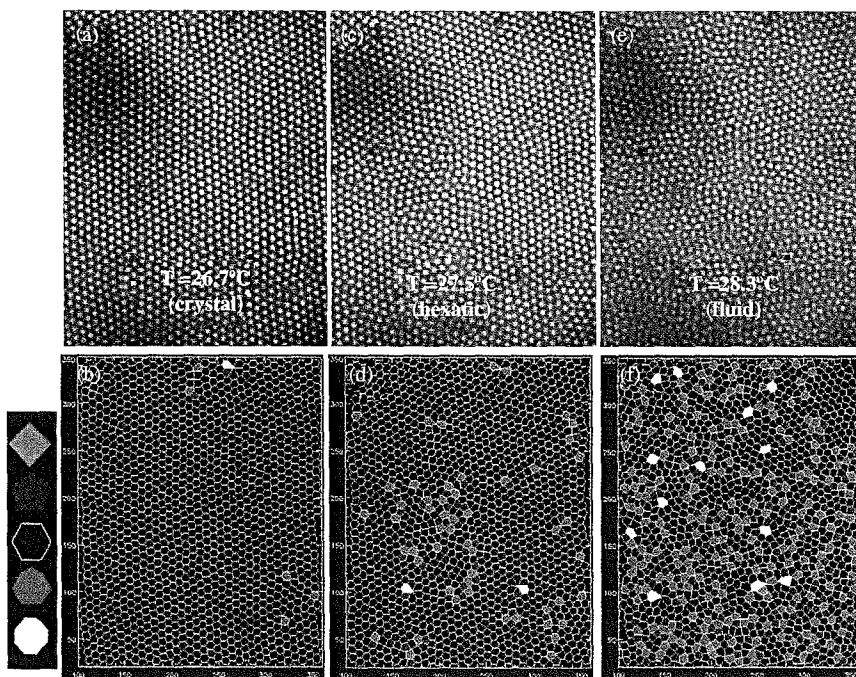
Figure 10.22 Real-space images of 2D NIPA microgel crystals at (a) crystal, (b) hexatic, and (c) liquid phases. (b,d,f) are the corresponding Voronoi diagrams of (a,c,e), respectively. Particles without six nearest neighbors are labeled by dark gray polygons.

The dense monolayers of 800 nm spheres formed crystal domains within the sample cell of typical size $(40\,\mu m)^2$, corresponding to $\sim$3000 particles. Measurements were carried out on a $(20\,\mu m)^2$ central area, well separated from the grain boundaries, see Figure 10.22a, c, and e. In practice, we found that grain boundaries affected only a few neighboring lines of particles and that melting started almost simultaneously throughout the crystal, both from inside the crystal domains and at the grain boundaries. This behavior differs qualitatively from grain-boundary melting in 3D [141] and edge melting in 2D [174], wherein the melting starts from grain boundaries or edges and then propagates into the crystal. Our observations suggest that the interfacial energies for liquid nucleation from within crystal domains might be similar to those of liquid nucleation starting from grain boundaries.

10.4.4
Data Analysis

Figure 10.23 shows typical particle trajectories in the three phases. From the $g_6(r)$ shown in Figure 10.24a, we can semiquantitatively distinguish three regimes corresponding to crystal, hexatic, and liquid as predicted by KTHNY theory: $g_6(r) \sim$ constant (long-range orientational order) for 26.5–26.9 °C, $g_6(r) \sim r^{-\eta_{6r}}$
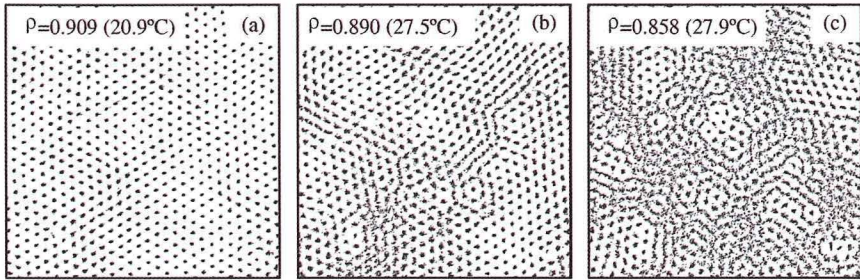
Figure 10.23 Typical 10-s particle trajectories in the (a) crystal, (b) hexatic, and (c) liquid phases, respectively.

(quasi-long-range order) for 27.1–27.5 °C, and $g_6(r) \sim e^{-r/\xi_6}$ (short-range order) for 27.7–28.5 °C. These three regions are more clearly resolved over three decades of dynamic range in Figure 10.24c and d, which plots the dynamic quantity $g_6(t)$. Comparing Figure 10.24a and c, we confirm KTHNY predictions [207] that the power
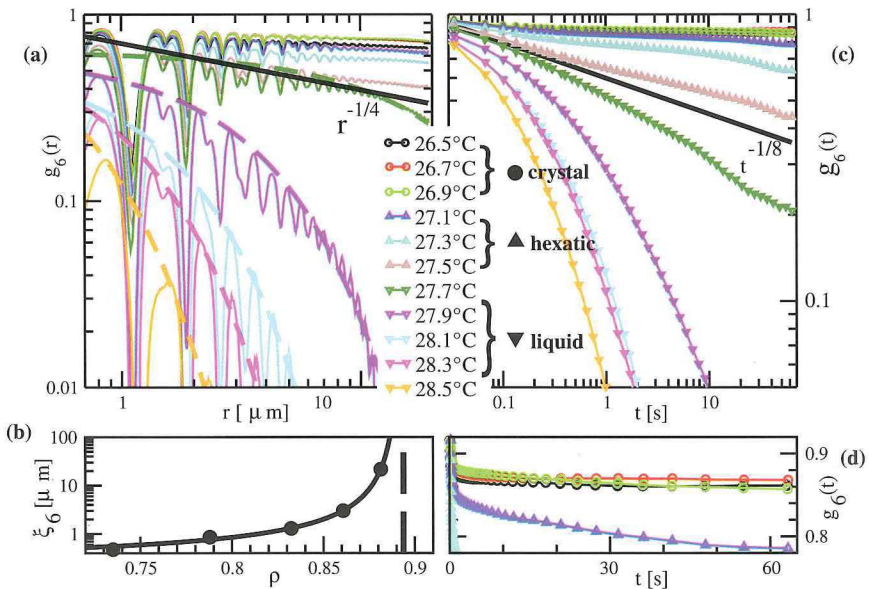
Figure 10.24 (a) Orientational correlation functions $g_6(r)$. Minima in the oscillations are associated with off-lattice site particles. The five dashed curves are fits of $g_6(r)$ to e^{-r/ξ_6}. $r^{-1/4}$ is the KTHNY prediction at hexatic–liquid transition point. (b) Circles are the orientational correlation lengths ξ_6 obtained from the fits in (a). The solid curve is a fit to the KTHNY prediction $\xi_6(\varrho) \propto e^{-b_\xi/\sqrt{\varrho_i-\varrho}}$ with $b_\xi = 0.566$ and $\varrho_i = 0.894$. These fit values, however, are prone to systematic error as a result of finite size effects [239]. (c) The orientational correlation function $g_6(t)$ in time. $t^{-1/8}$ is the KTHNY prediction at hexatic–liquid transition point. (d) Expanded version of (c) that more clearly exhibits the transition from long-range to quasi-long-range order. The 11 temperatures correspond to the 11 densities in Figure 10.25.

law decay of $g_6(t)$ is two times slower than that of $g_6(r)$, and $2\eta_{6t} = \eta_{6r} = 1/4$ at the hexatic–liquid transition point. $g_T(t)$ and $g_T(r)$ yielded consistent results. We observed that $g_T(t) \sim t^{-\eta}$ (crystal) for $T < 27\ ^\circ$C and $g_T(t) \sim e^{-t/\tau}$ (hexatic and liquid) for $T > 27\ ^\circ$C. The KTHNY prediction that $\eta_{Tr} = 1/3$ [207] at the crystal hexatic transition point was also confirmed. The oscillations in $g_6(r)$ and $g_T(r)$ correspond to the oscillations in radial distribution function $g(r)$: the off-lattice particles usually have lower probability in $g(r)$, lower $|\psi_6|$, and less correlation with other particles.

Despite substantial agreement with the KTHNY model, two major ambiguities arise in the traditional correlation function analysis: (i) the power law decay of g_6 can reflect crystal–liquid coexistence rather than the hexatic phase and (ii) finite size and finite time effects introduce ambiguities into the correlation function curve shapes near transition points. For example, the $T = 27.7\ ^\circ$C curve in Figure 10.24c appears to decay algebraically over the finite measured timescale, but it could also decay exponentially at longer times. Since the curve appears below the theoretical $t^{-1/8}$ transition curve, we assigned the system to the liquid phase.

Other correlation functions, such as the spatial density autocorrelation function $g(r)$, that is the radial distribution function, and the 2D structure factor $s(k)$ can also be used to determine the phase transition point [225, 226]. In our experiments, however, these methods appeared to have more ambiguities [159] because the theoretical functional forms of different phases are very similar close to the phase transition points.

Another function of interest is the Lindemann parameter L that is a measure of the particle mean-square fluctuation. It has been used as a traditional criterion of melting. For 2D melting, however, L diverges slowly even in the crystal phase due to strong long-wavelength fluctuations in 2D. To avoid such divergences, we calculated the *dynamic* Lindemann parameter L in a local coordinate system based on the neighbor positions [229, 239a]. It is defined as a bond length fluctuation, that is,

$$L^2 = \frac{\langle(\Delta \mathbf{r}_{\text{rel}}(t))^2\rangle}{2a^2} = \frac{\langle(\Delta \mathbf{u}_i(t) - \Delta \mathbf{u}_j(t))^2\rangle}{2a^2} \tag{10.13}$$

where $\Delta \mathbf{r}_{\text{rel}}$ is the relative neighbor–neighbor displacement, $\Delta \mathbf{u}_i$ is the displacement of particle i, and particles i and j are nearest neighbors. As shown in Figure 10.25, L^2 converges below 27 °C; in this case, particles remain close to their lattice sites. Divergence of L^2 is found above 27 °C; in this case, particles can more readily exchange positions with their neighbors via the gliding and climbing of disloca-tions [207]. This transition at 27 °C is also consistent with our direct measurement of dislocation densities (see discussion below) in Figure 10.26a.

Defect densities are helpful for distinguishing different phases. The Voronoi diagram in Figure 10.22b, d, and f shows typical defects in the three phases. Particles with $n_n \neq 6$ are considered to be defects. KTHNY theory suggests that the creation of *free* dislocations (isolated 5–7 pairs) drives the system from crystal to hexatic phase, and the creation of *free* disclinations (isolated $n_n = 5$ or 7 defects) drives the transition from hexatic to liquid phase. We measured defect concentrations as a function of
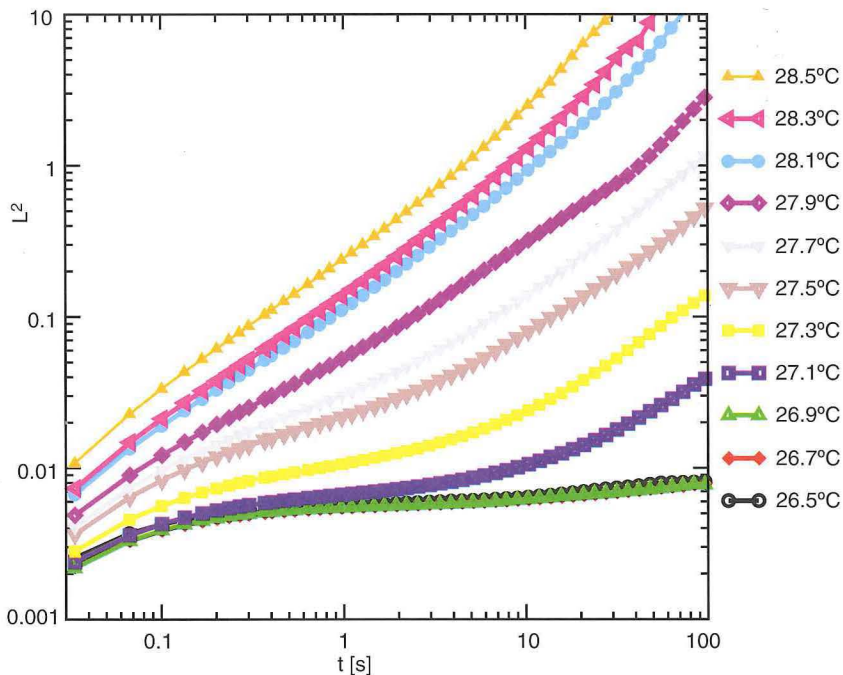
Figure 10.25 Square of dynamic Lindemann parameters at 11 temperatures.

temperature. Figure 10.26a shows that dislocations start to appear for $T > 27$ °C ($\varrho_m = 0.905$), and disclinations start to appear for $T > 27.7$ °C ($\varrho_i = 0.875$). Although defect density measurements are less sensitive to finite size effects than the correlation functions [239], the assignment of melting volume fraction ϱ_m based on defect density (Figure 10.26a) is somewhat problematic too. Problems can arise because (1) the data (Figure 10.26a) inevitably includes dislocations that are not completely "free", for example, dislocation pairs in Figure 10.27a that are nearly adjacent to one another, point in opposite directions, and thus give zero Burgers vector for a large Burgers circuit; (2) the data (Figure 10.26a) are susceptible to other systematic errors, for example, miscounting large defect clusters equivalent to a free dislocation, for example, a "free" 6-mer 5-7-5-7-5-7. In fact, Figure 10.26a very likely overestimates ϱ_m because sufficient numbers of "nonfree" dislocations are needed before the dislocation chemical potential reaches zero and free dislocations are produced. Consequently, a dislocation precursor stage in the crystal phase might be expected.

Note that the densities of $5n_n$ and $7n_n$ are the same only in perfect crystals with periodic boundary conditions if neglecting $n_n = 3, 4, 8 \ldots$ defects [207]. In the experiment, we observed a density imbalance of $5n_n$ and $7n_n$ in Figure 10.26a because (1) our polycrystals have "free" boundary conditions, thus $5n_n$ and $7n_n$ can be generated not only by pair but also by diffusing from boundaries [159, 207]; (2) any deviation from the strict monolayer limit can produce a concentration
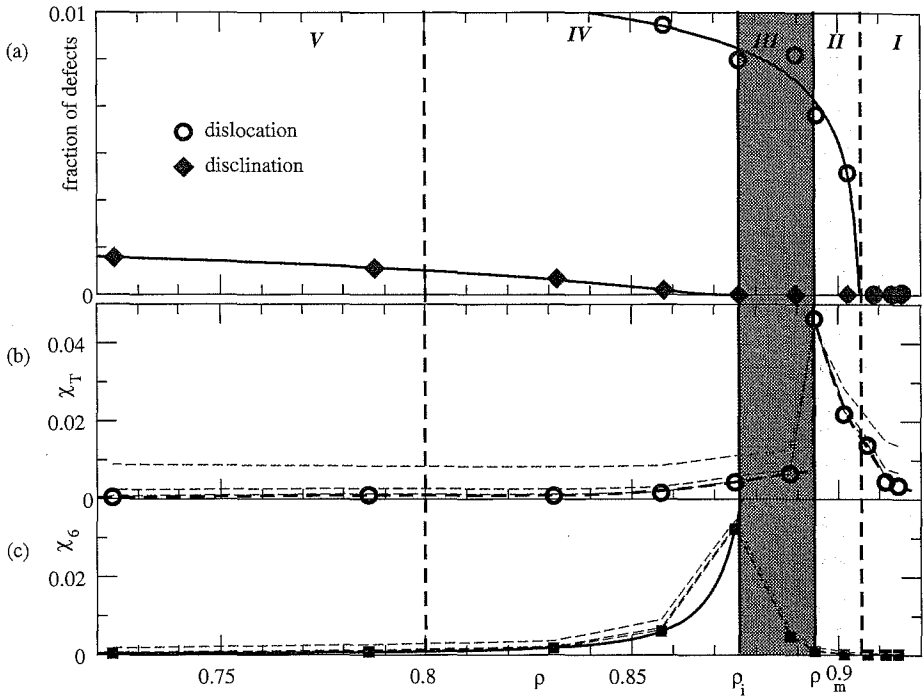
Figure 10.26 (a) Thick dashed curve: $n_n = 5$ disclination density. Thin dashed curve: $n_n = 7$ disclination density. Diamonds: net disclination density; circles: dislocation density fit by $e^{-2b_m/(\varrho_m - \varrho)^{0.36963}}$ [207]. (b) Translational and (c) orientational susceptibilities. Dashed curves: χ_L derived from subbox sizes $L = 5, 10, 20\,\mu m$ from top to bottom. Symbols: χ_∞ extrapolated from dashed curves. The solid curve in (c) is a fit to the KTHNY prediction [237] $\chi_6(\varrho) \propto e^{-b_\chi/\sqrt{\varrho_i - \varrho}}$ with $\varrho_i = 0.901$ and $b_\chi = 1.14$. Vertical solid lines partition crystal (regions I and II), hexatic (region III), and liquid (regions IV and V) phases as determined from susceptibilities in (b) and (c). Region II is a "dislocation precursor stage" of crystal with dislocations. Region IV is a prefreezing stage [242] of liquid with ordered patches.
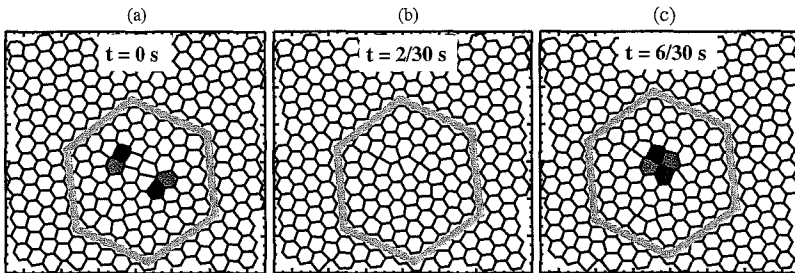
Figure 10.27 Voronoi diagram of the time evolution of a nonfree dislocation pair at 27.1 °C. Dark and light polygons represent particles with 5 and 7 nearest neighbors, respectively. (a–c) All yield zero Burgers vector as shown by the closed hexagonal loop. Dislocations can rapidly form and annihilate in pairs if they are in the same lattice line.

asymmetry [207]; (3) the observed higher density of $n_n = 8, 9$ than $n_n = 3, 4$ defects partially compensated the imbalance. The higher density of $5n_n$ reflects their lower free energy compared to that of $7n_n$. Besides the static properties noted above, we observed some interesting defect dynamics. For example, dislocations often dissociated from larger defect clusters (e.g., 6-mer 5-7-5-7-5-7) rather than from isolated pairs of dislocations (5-7-5-7 quartet), perhaps because the energy change for such disassociation is small.

In order to avoid the ambiguities outlined above and determine the true ϱ_m, we explored the utility of using the order parameter susceptibility, χ, for finding phase transition points. χ is a measure of the fluctuations of the order parameter in 9000 frames. To ameliorate finite size effects, we calculated χ_L in different size subboxes within the sample (dashed curves in Figure 10.26b and c)) and then extrapolated to χ_∞, thus attaining the thermodynamic limit (see Ref. [159] for details). The sharp divergence/discontinuity of $\chi_{T\infty}$ and $\chi_{6\infty}$ in Figure 10.26b and c clearly indicates the two transitions of the melting process. Although the magnitude of χ suffered from size effects, the diverging point of χ was robust to box size. Thus, the susceptibility method avoided finite-size ambiguities. The divergence of χ also avoids ambiguities arising from the similar functional forms of other measures (e.g., correlation functions) near transition points. Theoretically, we expect the divergence of χ to have better statistics than correlation function shape because χ is essentially an integral of the correlation function. We also observed that the diverging points of χ_T were robust to small uncertainties in **G**, though the exact magnitude of χ_T was somewhat sensitive to **G**.

10.4.5
The Hexatic Phase and Other Features of the Phase Diagram

We clearly observed the middle hexatic phase that has short-ranged translational order, quasi-long-range orientational order, zero disclination density, and finite dislocation density. Furthermore, we resolve five regimes that are marked off in Figure 10.26 based on the various analyses we have carried out. Region I is crystalline with few dislocations (Figure 10.26a), convergent dynamic Lindemann parameters over the measured timescales (Figure 10.25), constant $g_6(r), g_6(t)$ (Figure 10.24), and algebraic decay of $g_T(t)$. We take region II to be a "dislocation precursor stage" in the crystal because dislocations have started to appear, but their density is not high enough for the system to reach the hexatic phase, wherein the chemical potential of dislocation reaches zero. In other words, the observed dislocations in region II are not "free." This gas of nonfree dislocations causes a softening of the crystal, an effect that has been observed in the crystal phase [240, 241]. The dynamic Lindemann parameter is divergent in region II, a direct consequence of the nonzero dislocation density that permits particles near dislocations to diffuse out of their cages via the gliding and climbing [207] of dislocations. The correlation function, $g_6(t)$, has finite-size ambiguity in region II. For example, the $T = 27.1\ °C$ curve in Figure 10.24d appears to have lost orientational order over the measured timescale, but could become constant at longer times. Region III is the hexatic phase as determined from

the χ measurements and other analyses. In region IV, disclinations start to appear (Figure 10.26a), and $g_6(r)$, $g_6(t)$ decay exponentially (Figure 10.24). We take region IV to be a "prefreezing" liquid [242] because it has visible ordered patches. The nonzero ψ_6, the splitting of the second peak in $g(r)$, and the hexagonal shape of the structure factor $s(k)$ in region IV are also indicative of the presence of ordered patches. Region V is the liquid phase.

10.4.6
The Order of the Phase Transitions

The order of the phase transition can, in principle, be deduced from the shape of susceptibility curves. If the curve on the left of the diverging point and the curve on the right of the diverging point have the same asymptotic ϱ, then the transition is second order; otherwise, it is first order [243]. The curve shape in Figure 10.26b and c are consistent with second-order transitions. However, the χ_T curve shape is sensitive to the choice of **G** even though the diverging point is quite robust. For the liquid hexatic transition in Figure 10.26c, when we fit the left part (liquid regime) of the curve with the KTHNY prediction, we obtained an unreasonably high asymptotic transition density $\varrho_i = 0.901$ as obtained in Ref. [219]. This discrepancy suggests the hexatic–liquid transition may be more first-order-like. In addition, the continuous phase transitions must satisfy universality relations, while first-order transitions need not. Our $b_{6\xi} = 0.566$, from Figure 10.24b, and $b_{6\chi} = 1.14$, from Figure 10.26c, do not completely satisfy the universality [237] $b_{6\chi} = (2-\eta_6)b_{6\xi}$ where $\eta_6 = 1/4$. This failure could be viewed as further evidence of a first-order transition; however, when we forced $b_{6\chi}$ and $b_{6\xi}$ to satisfy the universality relation, they still gave somewhat reasonable (albeit worse) fitting curves because other fitting parameters were adjustable too. For example, the five data points in Figure 10.24b can be fit well by the other two free parameters when $b_{6\xi}$ is fixed. In total, the evidence leans slightly to favor a first-order liquid hexatic transition, but is not sufficient to unambiguously exclude a second-order transition. Future work with finer control of the approach to the phase transition should enable us to pin down the order of two transitions more precisely.

10.4.7
Summary

In summary, we used the divergence of susceptibilities to determine the phase transition points of a 2D microgel suspension during the melting process. This approach avoided ambiguities from finite-size effects, and the diverging points were robust. We clearly observed the hexatic phase in a system of particles interacting via short-range soft repulsion potentials. Five regimes were assigned to the phase diagram in Figure 10.26. A number of KTHNY predictions were quantitatively confirmed, especially near the hexatic–liquid transition, but the order of two phase transitions was not unambiguously resolved due to our limited temperature resolution.

10.5
**Geometric Frustration in Colloidal "Antiferromagnets"**

10.5.1
Background

Geometric frustration is a phenomenon that arises when lattice structure prevents simultaneous minimization of local interactions. Arguably the most famous example of geometric frustration arises in the context of antiferromagnetic (AF) materials. AF Ising spins on a 2D triangular lattice have strong geometric frustration. The problem was famously studied by Wannier in 1950 [244, 245]. Consider three spins on a triangle shown in Figure 10.29a. When two spins are arranged to be antiparallel to satisfy their antiferromagnetic interaction, the third one has no way to be antiparallel to both of the other spins. Thus, it is impossible to simultaneously satisfy all nearest-neighbor interactions on a triangular lattice. In contrast, antiferromagnetic Ising spins on a square lattice have no geometric frustration because every spin can be antiparallel to all four of its nearest neighbors (see Figure 10.28b). Frustration leads to materials with many degenerate ground states. Figure 10.28c is one possible ground state with a striped configuration wherein each triangular plaquette has two satisfied bonds and one frustrated bond, and Figure 10.28d and e denotes more general ground-state configurations. By removing all frustrated bonds and drawing in all satisfied bonds only in the latter configuration, the ground state can be viewed as a stack of cubes (see Figure 10.28f and g) [246]. The ground states and cube stacks have one-to-one correspondence, thus there are many possible ground states because there are many ways to pack cubes.

For the 2D triangular lattice, there are $W \simeq e^{0.3231N}$ ground states [244, 245], and thus the system has an extensive entropy at zero temperature, that is, $S \simeq 0.3231Nk_B$, where N is the number of spins in the system. The triangular lattice antiferromagnet is the only geometrically frustrated 2D Bravais lattice, and it therefore plays an important role within the theory of cooperative phenomenon in 2D. However, although the model outlined above is a prototypical frustrated magnet, progress studying it has suffered from a lack of experimental realization.

Broadly speaking, geometric frustration arises in many physical and biological systems [247] ranging from water [248] and spin ice [249] to magnets [250–252], ceramics [253], and high-T_c superconductors [254]. Traditionally, these phenomena have been explored in atomic materials by ensemble averaging techniques such as neutron and X-ray scattering, muon spin rotation, nuclear magnetic resonance, and heat capacity and susceptibility measurements [252, 253]. Artificial arrays of mesoscopic constituents have also been fabricated to probe geometric frustration at the single-"particle" level. Examples of the latter include Josephson junctions [255, 256], superconducting rings [257, 258], ferromagnetic islands [259], and recent simulations [260] of charged colloids in optical traps. Observations in these model systems, however, have been limited to the static patterns into which these systems freeze when cooled. Thus, many questions about frustrated systems remain unexplored, particularly those associated with single-particle dynamics.
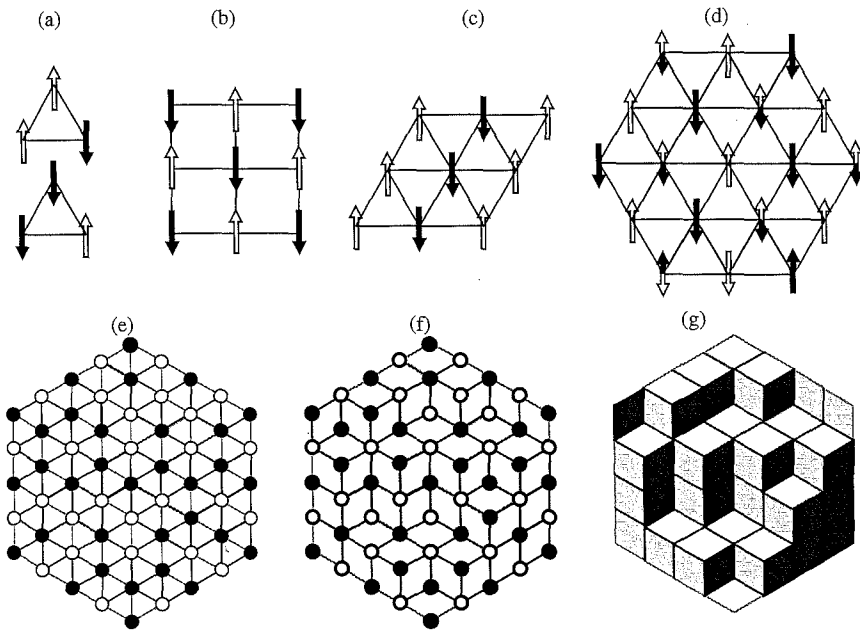
Figure 10.28 Schematics of ground states antiferromagnetic Ising spin 2D lattices. (a) The ground state of AF spins in triangular unit lattices, each triangle has two satisfied and one frustrated bonds. (b) The ground state of AF spins in a square lattice. All bonds (nearest-neighbor interactions) are satisfied. (c) One possible ground state of triangular AF spin lattice with a striped configuration. (d) A more general ground state, the up–down arrows represent spins that are surrounded by three up and three down spins, thus each of them can be up or down. The configuration shows that the ground state is highly degenerate. (e) Another ground-state configuration, each triangular plaquette has one frustrated and two satisfied bonds. Here, open (closed) circle denotes as up (down) state. (f) The same configuration of (e) where only satisfied bonds are shown. (g) Rhombuses in (f) with three orientations are painted by three gray scales so that the ground state can be better viewed as a cube stack.

The buckled colloidal monolayer provides an elegant model system for measuring the *single-spin* static and *dynamical* properties of a geometrically frustrated system. It is readily constructed by confining colloidal spheres between two parallel walls. When the wall separation is about 1.5 sphere diameter, the particles assemble (at high packing fraction) into a buckled triangular lattice with either up or down displacements analogous to an antiferromagnetic Ising model on a triangular lattice. Buckling minimizes system free energy $F = U-TS$, where U is the internal energy, T is temperature, and S is the entropy; spheres move apart to lower their repulsive interaction potential energy U and to increase their free volume V, which in turn leads to an entropy increase with $S \propto \ln V$. The effective repulsion causes spheres to move to the top or bottom sample wall. Nearest neighbors maximize free volume by moving to opposite walls (see Figure 10.29b). Furthermore, by using microgel spheres, the effective antiferromagnetic interactions can be tuned by
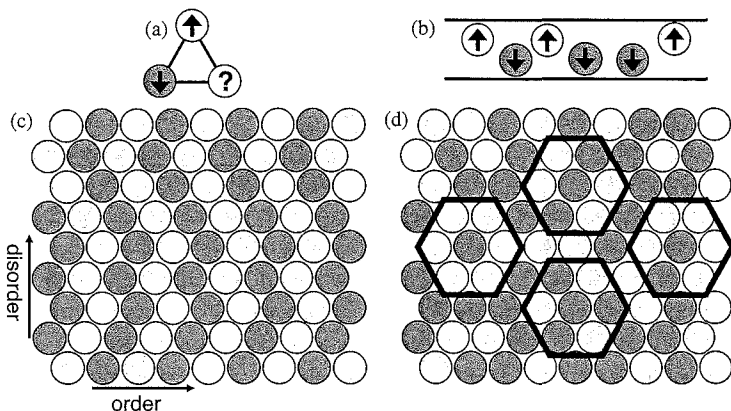
Figure 10.29 (a) Three spins on a triangular plaquette cannot simultaneously satisfy all AF interactions. (b) For colloids confined between walls separated of order 1.5 sphere diameters (side view), particles move to opposite walls in order to maximize free volume. (c and d) Ising ground-state configurations wherein each triangular plaquette has two satisfied bonds and one frustrated bond. (c) Zigzag stripes generated by stacking rows of alternating up/down particles with random side-wise shifts; all particles have exactly two frustrated neighbors. (d) Particles in disordered configurations have zero, one, two, or three frustrated neighbors (gray hexagons).

changing microgel particle diameter, and therefore the samples can be driven from spin liquid to glassy states. Once again, this class of colloid experiment provides access to new physics, in this case bridging the fields of frustrated magnetism and soft matter.

Buckled colloidal monolayers were first observed more than two decades ago [233, 261, 262], and the AF analogy was then suggested [262, 263]. On the basis of Koshikiya and Hachisu's colloidal monolayer image [263], Ogawa suggested the AF analogy and estimated the probabilities of different local configurations in ground state. However, image analysis was not readily available in the 1980s limiting the quantitative study of the experiment. To date, few quantitative measurements have been performed on this system class, and the themes explored by most of the early work centered largely on structural transitions exhibited by colloidal thin films as a function of increasing sample thickness [233, 262, 264, 265], rather than their connection to frustrated antiferromagnets. In a wedged sample, the following sequence of crystal phases has been observed as a function of increasing wall separation [262]: monolayer triangular lattice, buckled monolayer (i.e., our configuration), two-layer square lattice, two-layer triangular lattice, three-layer square lattice, three-layer triangular lattice, and more. Simulations studied the nature of these solid–solid phase transitions and provided quantitative phase diagrams for hard spheres [220, 266, 267]. Usually, the crystal domain size formed by traditional colloids is not large, however [233, 262, 263, 265]. The diameter tunable spheres permit us to anneal the buckled crystals near the melting point and form larger crystals with better quality.
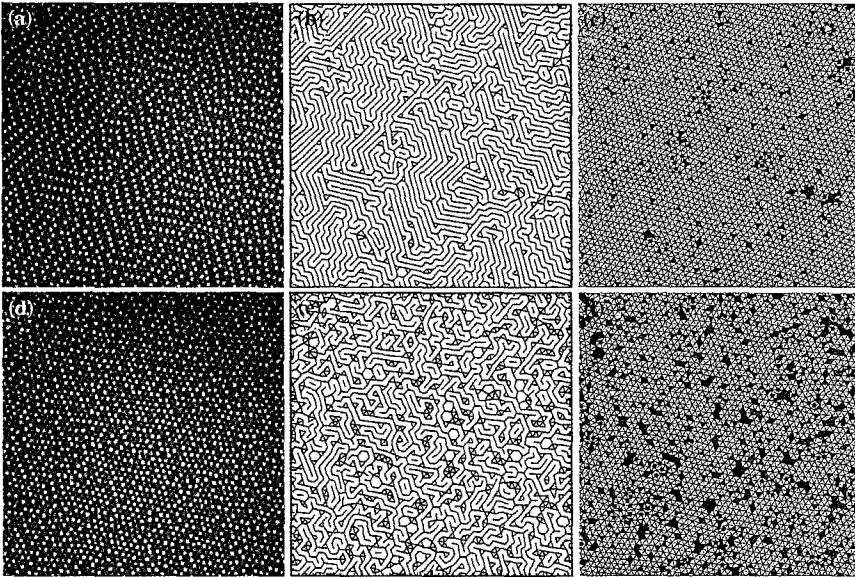
Figure 10.30 Buckled monolayer of colloidal spheres. $(32\,\mu m)^2$ area at $T = 24.7\,°C$ (a–c) and $27.1\,°C$ (d–f). Bright spheres: up; dark spheres: down. (b and e) Labyrinth patterns obtained by drawing in only the frustrated up–up (dark gray) and down–down (light gray) bonds. (c and f) Corresponding Delaunay triangulations. Black dots mark defects in the triangular lattice, that is, particles without six nearest neighbors. Thermally excited triangles with three spheres up/down are labeled by dark gray/light gray.

10.5.2
The Experimental System

The experiments employ densely packed spheres confined by parallel glass walls. Microgel spheres are cross-linked with PMMA (polymethyl methacrylate) at their surfaces to prevent sticking to glass walls. For walls separated by a distance of about 1.5 sphere diameter, the particles maintain in-plane triangular order but buckle out of plane (see Figure 10.30a and d). Samples were equilibrated at low volume fraction near the melting point to produce 2D crystal domains with $\sim 10^4$ spheres covering an area of order $(60\,\mu m)^2$. Video microscopy measurements were carried out far from grain boundaries on a $\sim (32\,\mu m)^2$ central area ($\sim$2600 spheres) within the larger crystal domain. Below $24\,°C$, the system is jammed and no dynamics is observed and above $27.5\,°C$ the in-plane crystals melt. Our primary measurements of the frustrated states probe five temperatures in between, from 24.7 to 27.1 $°C$ in 0.6 $°C$ steps. In this range, the hydrodynamic diameter of the particles decreases linearly with temperature from $0.89\,\mu m$ to $0.76\,\mu m$, while the average in-plane particle separation remains constant. We slowly cycled through this temperature range and hysteresis was not observed.

10.5.3
Antiferromagnetic Order

Typical frustrated samples are illustrated in Figure 10.30. Figure 10.30a and d shows roughly half of the spheres as bright because they are in the focal plane of the microscope; the other half, located close to the bottom plate, are slightly out of focus and appear darker. To analyze these images, we discretize the continuous brightness profile of the particles into two Ising states with $s_i = \pm 1$ (see Figure 10.30).

The nature of the frustrated states can be exhibited in different ways in processed images based on the data in Figure 10.30a and d. One way focuses on the "bonds" between particles. We refer to the line connecting a pair of neighboring particles in opposite states ($s_i s_j = -1$) as a satisfied bond, that is, a bond that satisfies the effective AF interaction, and we refer to the line connecting up–up or down–down pairs (with $s_i s_j = 1$) as a frustrated bond. Images of these bonds (Figure 10.30b and e) show that the frustrated bonds form an almost single-line labyrinth (Figure 10.30b) at low temperature that then form small domains (Figure 10.30e) at high temperature. AF order can also be characterized by the average number, $\langle N_f \rangle$, of frustrated bonds per particle. In the limit of weak interactions, that is, $T \to \infty$, an Ising system will choose a completely random configuration with half of the six bonds satisfied and half frustrated, leading to $\langle N_f \rangle = 3$. In the limit of strong interactions, that is, $T = 0$, on the other hand, each triangular plaquette will have one frustrated bond (see Figure 10.29a), a third of the bonds are frustrated, and therefore $\langle N_f \rangle = 2$. $\langle N_f \rangle$ is essentially a linear rescaling of the density of excited triangles (3 up or 3 down) in Figure 10.30c and f, which ranges from 0 in the AF Ising ground state to 0.5 for a random configuration. By analyzing the experimental movies, we found that $\langle N_f \rangle$ decreased from approximately 2.5 to 2.1 in the temperature interval 27.1–24.7 °C (see Figure 10.31).

10.5.4
Stripes and the Zigzagging Ground State

Ideal geometrically frustrated systems are highly degenerate with extensive entropy at zero temperature. However, the third law of thermodynamics dictates that system
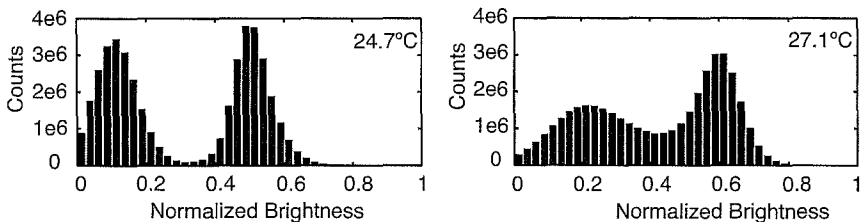
Figure 10.31 Histograms of particle brightness normalized to [0, 1]. The histogram has a bimodal distribution where ~50% of the particles were darker/brighter than the central minimum point for all temperatures.

entropy vanish as $T \rightarrow 0$. This suggests a problem with the Wannier model. Of course, the model is an idealization using a rigid lattice and including only nearest-neighbor interactions. In real materials, subtle effects, for example, anisotropic interactions [268], long-range interactions [269], boundary conditions [270], and lattice distortions [271, 272] can relieve frustration.

The partially ordered zigzagging striped sample observed at high volume fraction in Figure 10.30a and b is an example of a frustration relief by symmetry-reducing lattice distortions. In the colloidal monolayer, the triangular packing is self-assembled, and (like atoms in real solids) the particles are not forced to remain at fixed positions on the lattice [273]. This deformability, and the fact that the free volume of the system is a collective function of all particle positions, breaks the mapping to simple Ising models with pair-wise additive nearest-neighbor interactions. In short, the Ising ground state is a single-line labyrinth with $N_f = 0, 1, 2, 3$ and $\langle N_f \rangle = 2$, while the colloidal spheres' real ground state appears to be a subset of the Ising ground states, including nonbranching single-line labyrinths with $N_f = 2$ in the bulk.

We can understand zigzagging stripes as a ground state by viewing them as random stacks of ordered lines of alternating up and down states, see Figure 10.29c. Notice that the straight and zigzagging stripes are essentially a 2D analogy of the face-centered cubic and randomly hexagonal close packed (rhcp) [274] structures in 3D. Equal-sized spheres can be most efficiently packed in 3D by stacking hexagonal close-packed 2D layers, that is, fcc or rhcp. Ordered stacking as ABCABC... (fcc) or random stacking such as ABACB... (rhcp) has the same volume fraction, simply because nonneighbor layers cannot affect each other. For a similar reason, zigzagging stripes have the same high closed packing area fraction as the straight stripes. In Figure 10.29c, the disordered stack sequence is random along the vertical direction and hence yield $\sim 2^{\sqrt{N}}$ configurations. Consequently, the ground-state entropy $S \sim \sqrt{N}$ is subextensive.

10.5.5
Dynamics

Real-time videos permit direct visualization of "spin flipping", as well as the motions of thermal excitations and defects, in frustrated systems for the first time. The ability to track particle dynamics at the "single-spin" level will likely be the most important contribution of the colloid experiments to the frustration subfield. Thermal excitations, for example, labeled as colored triangles in Figure 10.30c and f were typically found to be generated/annihilated in pairs due to the flipping of a particle shared by the two triangles; isolated thermal excitations, on the other hand, appear to be quite stable. Similarly, if we simply follow the up–down spin trajectory of single particles, then we should obtain a range of interesting dynamics. An example of spin trajectory as a function of time is shown in Figure 10.32.

As the first step toward quantifying these effects, we first extract the full time spin trajectory, $s_i(t)$, of each particle i. In Figure 10.33b, the ensemble-averaged single-particle temporal spin autocorrelation function, that is,
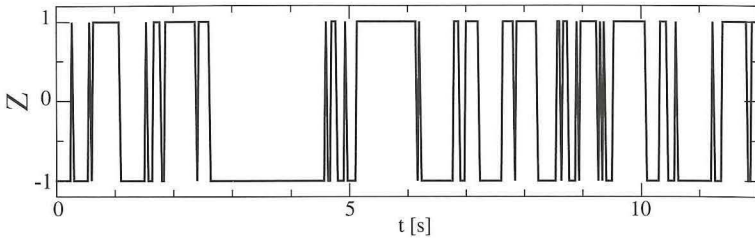
Figure 10.32 A typical trajectory of a single "spin" flip. + (−) 1 denotes an up (down) Ising state.

$$C(t) = [\langle s_i(t)s_i(0)\rangle - \langle s_i\rangle^2]/[\langle s_i^2\rangle - \langle s_i\rangle^2] \tag{10.14}$$

is plotted as a function of temperature. The function is averaged over all particles that are not located at lattice defects. The correlation function cannot be well fitted by a power law or an exponential, but it can be fit to a stretched exponential form, that is, $C(t) = \exp[-(t/\tau)^\beta]$. The measured relaxation time τ exhibits a dramatic increase as the particles swell at low temperature, while the extracted stretching exponent β decreases.

This behavior is suggestive of dynamics similar to those found in glasses. We speculate that particles in the frustrated system experience a complex energy landscape wherein transitions between different local configurations have different
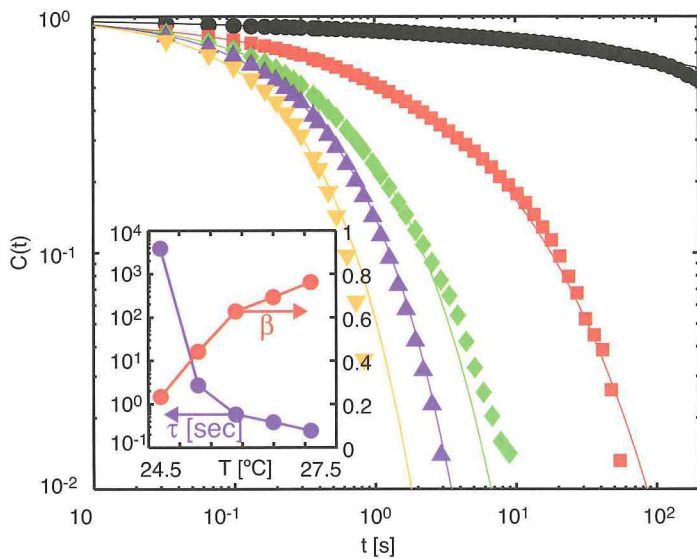
Figure 10.33 Single "spin" autocorrelation functions (Equation 10.14 averaged over all particle trajectories. Lines are fits to stretched exponentials $C(t) = \exp[-(t/\tau)^\beta]$, with τ and β given in the inset.

energy barriers and decay rates. It is not clear why the final averaged autocorrelation function can be fitted so economically by a simple stretched exponential form with only two free parameters. The stretched exponential behavior has been referred to as "one of Nature's best-kept secrets [275]," and it is possible that these geometrically frustrated colloids, with measurable single-particle dynamics, could once again provide a fresh platform from which to tackle this interesting challenge. For example, it should be possible to measure the correlation functions and flip rates of spins sitting in different local environments. We have begun computations along these lines [160].

Finally, in a different vein, defects in the underlying lattice can strongly affect the properties of frustrated systems. However, detailed knowledge about the role of defects in frustrated systems is very limited. Our experiments permit us to directly visualize defects nucleating, annihilating, and diffusing, see Figure 10.30c and f. By comparing trajectories containing different numbers and types of defects, our initial studies suggest that defect particles have faster in-plane diffusion and slower flipping dynamics than the average of the particles with six nearest neighbors.

10.5.6
Summary

We have demonstrated two-dimensional colloidal frustrated antiferromagnets. Colloidal microgel spheres with tunable diameter self-assemble to buckled mono-layer crystals and form a system analogous to the triangular lattice antiferromagnetic Ising model. By tuning volume fraction, we found that at high compaction, in-plane lattice deformation relieves most frustration and yields a zigzag stripe ground state with subextensive entropy. We measured spatial correlations and the statistics of various local configurations as well as their flipping rates and found strong dependences on arrangements of neighboring particles. As the glassy phase is approached, we observed dramatic slowing of the dynamics and formation of stretched exponential correlation functions. Single-defect dynamics were directly visualized and measured for the first time. The new system opens the door for the study of detailed single-particle dynamics in frustrated systems and begins an exploration of the connections between the frustrated soft materials and the more studied frustrated magnetic and related materials.

10.6
Future

Many more directions for fundamental physics experiments with NIPA microgel particles should be explored. Interesting new model systems will be created in the future. For example, very recent experiments have shown that NIPA particles are ideal for investigating thin-film melting [163b], 2D freezing [163b], jamming [163] and glassy behaviors [161, 162], dynamic heterogeneity, and even the crystal-to-glass transition. In principle, the microgel systems permit creation of frustration in other

contexts; for example, by filling thin cylinders with spheres, one can mimic a 1D chain of *xy*-spins [276]. Another exciting experimental arena, which need not even involve the development of new systems, concerns the perturbation and active manipulation of existing samples using laser tweezers and other tools. For example, potential energy landscapes for the particles can be created using laser tweezers of varying strength and periodicity (including rigid lattices), enabling experimenters to explore the role of lattice deformability on the dynamics and the creation of structure. Optical tweezers or magnetic traps can also be used to flip and to move individual spins, and video microscopy can be used to probe the resulting system's responses. Light beams can even be used to locally heat a region within the sample, causing the energy landscape to "reset" and permitting experimenters to understand different classes of response.

Indeed, research in this subfield of soft matter appears promising for years to come.

Acknowledgments

References

1 Hunter, R.J. (2001) *Foundations of Colloid Science*, 2nd edn, Oxford University Press.

2 Israelachvili, J.N. (1992) *Intermolecular and Surface Forces*, 2nd edn, Academic Press, London.

3 Daoud, M. and Williams, C.E. (1999) *Soft Matter Physics*, 1st edn, Springer, Germany.

4 Russel, W.B., Saville, D.A., and Schowalter, W.R. (1991) *Colloidal Dispersions*, 1st edn, Cambridge University Press, Cambridge.

5 Morrison, I.D. and Ross, S. (2002) *Colloidal Dispersions*, 1st edn, John Wiley & Sons, Inc., New York.

6 Larson, R.G. (1998) *The Structure and Rheology of Complex Fluids (Topics in Chemical Engineering)*, 1st edn, Oxford University Press, Oxford, New York.

7 Witten, T.A. and Pincus, P.A. (2004) *Structured Fluids: Polymers, Colloids, Surfactants*, 1st edn, Oxford University Press, New York.

8 Joannopoulos, J.D., Johnson, S.G., Winn, J.N., and Meade, R.D. (2008)

Photonic Crystals: Molding the Flow of Light, 2nd edn, Princeton University Press.

9 Holland, B.T., Blanford, C.F., and Stein, A. (1998) *Science*, **281**, 538.

10 Imhof, A. and Pine, D.J. (1997) *Nature*, **389**, 948.

11 Subramania, G., Constant, K., Biswas, R., Sigalas, M.M., and Ho, K. (1999) *Appl. Phys. Lett.*, **74**, 3933.

12 Velev, O.D., Tessier, P.M., Lenhoff, A.M., and Kaler, E.W. (1999) *Nature*, **401**, 548.

13 Vlasov, Y.A., Yao, N., and Norris, D.J. (1999) *Adv. Mater.*, **11**, 165.

14 Wijnhoven, J.E.G.J. and Vos, W.L. (1998) *Science*, **281**, 802.

15 Yablonovitch, E. (1999) *Nature*, **401**, 539.

16 Lopez, C. (2003) *Adv. Mater.*, **15**, 1679.

17 Xia, Y.N. and Whitesides, G.M. (1998) *Annu. Rev. Mater. Sci.*, **28**, 153.

18 Burmeister, F., Schafle, C., Keilhofer, B., Bechinger, C., Boneberg, J., and Leiderer, P. (1998a) *Adv. Mater.*, **10**, 495.

19 Hulteen, J.C. and Vanduyne, R.P. (1995) *Abstr. Pap. Am. Chem. Soc.*, **210**, 25.

20 Winzer, M., Kleiber, M., Dix, N., and Wiesendanger, R. (1996) *Appl. Phys. A: Mater.*, **63**, 617.

21 Burmeister, F., Schafle, C., Keilhofer, B., Bechinger, C., Boneberg, J., and Leiderer, P. (1998b) *Adv. Mater.*, **10**, 495.

22 Bhave, R.R. (1991) *Inorganic Membranes: Synthesis, Characteristics and Applications*, Van Nostrand Reinhold, New York.

23 Senkevich, J.J. and Desu, S.B. (1998) *Appl. Phys. Lett.*, **72**, 258.

24 Seino, H., Haba, O., Mochizuki, A., Yoshioka, M., and Ueda, M. (1997) *High. Perform. Polym.*, **9**, 333.

25 Kong, J., Franklin, N., Zhou, C., Chapline, M., Peng, S., Cho, K., and Dai, H. (2000) *Science*, **287**, 622.

26 Tanev, P.T., Chibwe, M., and Pinnavaia, T.J. (1994) *Nature*, **368**, 321.

27 Tennikov, M.B., Gazdina, N.V., Tennikova, T.B., and Svec, F. (1998) *J. Chromatogr. A*, **798**, 55.

28 Xie, S.F., Svec, F., and Frechet, J.M.J. (1997) *J. Chromatogr. A*, **775**, 65.

29 Lewandowski, K., Murer, P., Svec, F., and Frechet, J.M.J. (1998) *Anal. Chem.*, **70**, 1629.

30 Litovsky, E., Shapiro, M., and Shavit, A. (1996) *J. Am. Ceram. Soc.*, **79**, 1366.

31 Maquet, V. and Jerome, R. (1997) *Mater. Sci. Forum*, **250**, 15.

32 Palm, A. and Novotny, M.V. (1997) *Anal. Chem.*, **69**, 4499.

33 Peters, M.C. and Mooney, D.J. (1997) *Mater. Sci. Forum*, **250**, 43.

34 Deleuze, H., Schultze, X., and Sherrington, D. (1998) *Polymer*, **39**, 6109.

35 Akolekar, D.B., Hind, A.R., and Bhargava, S.K. (1998) *J. Colloid Interface Sci.*, **199**, 92.

36 Schugens, C., Maquet, V., Grandfils, C., Jerome, R., and Teyssie, P. (1996) *Polymer*, **37**, 1027.

37 Durkop, T., Getty, S.A., Cobas, E., and Fuhrer, M.S. (2004) *Nano Lett.*, **4**, 35.

38 Storhoff, J.J., Elghanian, R., Mucic, R.C., Mirkin, C.A., and Letsinger, R.L. (1998) *J. Am. Chem. Soc.*, **120**, 1959.

39 Bancel, S. and Hu, W.S. (1996) *Biotechnol. Prog.*, **12**, 398.

40 Elghanian, R., Storhoff, J.J., Mucic, R.C., Letsinger, R.L., and Mirkin, C.A. (1997) *Science*, **277**, 1078.

41 Lewis, J.A. (2000) *J. Am. Ceram. Soc.*, **83**, 2341.

42 Ray, S.S. and Bousmina, M. (2005) *Prog. Mater. Sci.*, **50**, 962.

43 Ray, S.S. and Okamoto, M. (2003) *Prog. Polym. Sci.*, **28**, 1539.

44 Tang, Z.Y., Kotov, N.A., Magonov, S., and Ozturk, B. (2003) *Nat. Mater.*, **2**, 413.

45 Baughman, R.H., Zakhidov, A.A., and de Heer, W.A. (2002) *Science*, **297**, 787.

46 Vigolo, B., Penicaud, A., Coulon, C., Sauder, C., Pailler, R., Journet, C., Bernier, P., and Poulin, P. (2000) *Science*, **290**, 1331.

47 Haggenmueller, R., Gommans, H.H., Rinzler, A.G., Fischer, J.E., and Winey, K.I. (2000) *Chem. Phys. Lett.*, **330**, 219.

48 Schadler, L.S., Giannaris, S.C., and Ajayan, P.M. (1998) *Appl. Phys. Lett.*, **73**, 3842.

49 Biercuk, M.J., Llaguno, M.C., Radosavljevic, M., Hyun, J.K.,

Johnson, A.T., and Fischer, J.E. (2002) *Appl. Phys. Lett.*, **80**, 2767.

50 Einstein, A. (1905) *Ann. Phys. Berlin*, **17**, 549.

51 Perrin, F. (1908) *C. R. Acad. Sci.*, **146**, 967.

52 Langevin, P. (1908) *C. R. Acad. Sci.*, **146**, 530.

53 Kubo, R. (1966) *Rep. Prog. Phys.*, **29**, 255.

54 Alder, B.J. and Wainwright, T.E. (1970) *Phys. Rev. A*, **1**, 18.

55 Mazur, P. and Oppenheim, I. (1970) *Physica*, **50**, 241.

56 Zwanzig, R. and Bixon, M. (1975) *J. Fluid Mech.*, **69**, 21.

57 Hinch, E.J. (1975) *J. Fluid Mech.*, **72**, 499.

58 Felderhof, B.U. (1978) *J. Phys. A: Math. Gen.*, **11**, 929.

59 Ermak, D.L. and Mccammon, J.A. (1978) *J. Chem. Phys.*, **69**, 1352.

60 Doi, M. and Edwards, S.F. (1978) *J. Chem. Soc. Faraday Trans. II*, **74**, 1789.

61 Jones, R.B. (1979) *Physica A*, **97**, 113.

62 Mazur, P. (1982) *Physica A*, **110**, 128.

63 Beenakker, C.W.J. and Mazur, P. (1983) *Physica A*, **120**, 388.

64 Beenakker, C.W.J. and Mazur, P. (1984) *Physica A*, **126**, 349.

65 Brady, J.F. and Bossis, G. (1988) *Annu. Rev. Fluid Mech.*, **20**, 111.

66 Granick, S. (1991) *Science*, **253**, 1374.

67 Jones, R.B. and Pusey, P.N. (1991) *Annu. Rev. Phys. Chem.*, **42**, 137.

68 Kaplan, P.D., Dinsmore, A.D., Yodh, A.G., and Pine, D.J. (1994) *Phys. Rev. E*, **50**, 4827.

69 Segre, P.N., Meeker, S.P., Pusey, P.N., and Poon, W.C.K. (1995) *Phys. Rev. Lett.*, **75**, 958.

70 Bedeaux, D. and Mazur, P. (1974) *Physica*, **76**, 247.

71 Batchelor, G.K. (1976) *J. Fluid Mech.*, **74**, 1.

72 Kao, M.H., Yodh, A.G., and Pine, D.J. (1993) *Phys. Rev. Lett.*, **70**, 242.

73 Zhu, J.X., Durian, D.J., Muller, J., Weitz, D.A., and Pine, D.J. (1992) *Phys. Rev. Lett.*, **68**, 2559.

74 Weitz, D.A., Pine, D.J., Pusey, P.N., and Tough, R.J.A. (1989) *Phys. Rev. Lett.*, **63**, 1747.

75 Qiu, X., Wu, X.L., Xue, J.Z., Pine, D.J., Weitz, D.A., and Chaikin, P.M. (1990) *Phys. Rev. Lett.*, **65**, 516.

76 Han, Y., Alsayed, A.M., Nobili, M., Zhang, J., Lubensky, T.C., and Yodh, A.G. (2006) *Science*, **314**, 626.

77 Asturnian, R.D. (1997) *Science*, **276**, 917.

78 Anderson, V.J. and Lekkerkerker, H.N.W. (2002) *Nature*, **416**, 811.

79 van der Kooij, F.M., Kassapidou, K., and Lekkerkerker, H.N.W. (2000) *Nature*, **406**, 868.

80 van Bruggen, M.P.B., van der Kooij, F.M., and Lekkerkerker, H.N.W. (1996) *J. Phys. Condens. Matter*, **8**, 9451.

81 Buining, P.A., Philipse, A.P., and Lekkerkerker, H.N.W. (1994) *Langmuir*, **10**, 2106.

82 Lekkerkerker, H.N.W. (1992) Disorder-to-Order Phase Tranitions in Concentrated Colloidal Dispersions, in *Structure and Dynamics of Strongly Interacting Colloids and Supramolecular Aggregates in Solution* (eds S. Chen, J. Huang, and P. Tartaglia), Kluwer Academic Publishers, p. 97.

83 Stroobants, A., Lekkerkerker, H.N.W., and Odijk, T. (1986) *Macromolecules*, **19**, 2232.

84 Lekkerkerker, H.N.W., Coulon, P., Haegen, V.D., and Deblieck, R. (1984) *J. Chem. Phys.*, **80**, 3427.

85 Lekkerkerker, H.N.W. and Stroobants, A. (1993) *Physica A*, **195**, 387.

86 Lekkerkerker, H.N.W., Buining, P., Buitnhuis, J., Vroege, G.J., and Stroobants, A. (1995) Liquid Crystal Phase Transitions in Dispersions of Rodlike Colloidal Particles in *Observation, Prediction and Simulation of Phase Transitions in Complex Fluids* (eds M. Baus, L.F. Rull, and J.P. Ryckaert), Kluwer Academic Publishers, pp. 53–112.

87 Poon, W.C.K. and Pusey, P.N. (1995) Phase Transitions of Spherical Colloids in *Observation, Prediction, and Simulation of Phase Transitions in Complex Fluids* (eds M. Baus, L.F. Rull, and J.P. Ryckaert), Kluwer Academic Publishers.

88 Pusey, P.N. and VanMegen, W. (1986) *Nature*, **320**, 340.

89 Crocker, J.C., Matteo, J.A., Dinsmore, A.D., and Yodh, A.G. (1999) *Phys. Rev. Lett.*, **82**, 4352.

90 Dinsmore, A.D., Warren, P.B., Poon, W.C.K., and Yodh, A.G. (1997) *Europhys. Lett.*, **40**, 337.

91 Adams, M., Dogic, Z., Keller, S.L., and Fraden, S. (1998) *Nature*, **393**, 349.

92 Dogic, Z. and Fraden, S. (1997) *Phys. Rev. Lett.*, **78**, 2417.

93 Dogic, Z., Frenkel, D., and Fraden, S. (2000) *Phys. Rev. E*, **62**, 3925.

94 Dogic, Z. and Fraden, S. (2000) *Langmuir*, **16**, 7820.

95 Dogic, Z., Purdy, K.R., Grelet, E., Adams, M., and Fraden, S. (2004) *Phys. Rev. E*, **69**, 051702. (a) Grier, D.G. (2003) *Nature*, **424**, 810. (b) Prasad, V., Semwogerere, D., and Weeks, E.R. (2007) *J. Phys. Cond. Matt.*, **19**, 113102.

96 Crocker, J.C. and Grier, D.G. (1996) *J. Colloid Interface Sci.*, **179**, 298.

97 Lau, A.W.C., Lin, K.H., and Yodh, A.G. (2003a) *Phys. Rev. E*, **66**, 020401.

98 Dinsmore, A.D., Yodh, A.G., and Pine, D.J. (1995) *Phys. Rev. E*, **52**, 4045.

99 Berthier, L., Biroli, G., Bouchaud, J.P., Cipelletti, L., Masri, D.E., L'Hote, D., Ladieu, F., and Pierno, M. (2005) *Science*, **310**, 1797.

100 Leunissen, M.E., Christova, C.G., Hynninen, A.P., Royall, C.P., Campbell, A.I., Imhof, A., Dijkstra, M., van Roij, R., and van Blaaderen, A. (2005) *Nature*, **437**, 235.

101 Yethiraj, A. and van Blaaderen, A. (2003) *Nature*, **421**, 513.

102 Nikolaides, M.G., Bausch, A.R., Hsu, M.F., Dinsmore, A.D., Brenner, M.P., Weitz, D.A., and Gay, C. (2002) *Nature*, **420**, 299.

103 Dinsmore, A.D., Hsu, M.F., Nikolaides, M.G., Marquez, M., Bausch, A.R., and Weitz, D.A. (2002) *Science*, **298**, 1006.

104 Pham, K.N., Puertas, A.M., Bergenholtz, J., Egelhaaf, S.U., Moussaid, A., Pusey, P.N., Schofield, A.B., Cates, M.E., Fuchs, M., and Poon, W.C.K. (2002) *Science*, **296**, 104.

105 Likos, C.N. (2001) *Phys. Rep.*, **348**, 267.

106 Trappe, V., Prasad, V., Cipelletti, L., Segre, P.N., and Weitz, D.A. (2001) *Nature*, **411**, 772.

107 Gasser, U., Weeks, E.R., Schofield, A., Pusey, P.N., and Weitz, D.A. (2001) *Science*, **292**, 258.

108 Lin, K.H., Crocker, J.C., Prasad, V., Schofield, A., Weitz, D.A., Lubensky, T.C., and Yodh, A.G. (2000) *Phys. Rev. Lett.*, **85**, 1770.

109 Xia, Y.N., Gates, B., Yin, Y.D., and Lu, Y. (2000) *Adv. Mater.*, **12**, 693.

110 Velev, O.D., Lenhoff, A.M., and Kaler, E.W. (2000) *Science*, **287**, 2240.

111 Weeks, E.R., Crocker, J.C., Levitt, A.C., Schofield, A., and Weitz, D.A. (2000) *Science*, **287**, 627.

112 Kegel, W.K. and van Blaaderen, A. (2000) *Science*, **287**, 290.

113 van Megen, W., Mortensen, T.C., Williams, S.R., and Muller, J. (1998) *Phys. Rev. E*, **58**, 6073.

114 Zhu, J.X., Li, M., Rogers, R., Meyer, W., Ottewill, R.H., Russell, W.B., and Chaikin, P.M. (1997) *Nature*, **387**, 883.

115 Harland, J.L. and van Megen, W. (1997) *Phys. Rev. E*, **55**, 3054.

116 van Blaaderen, A., Ruel, R., and Wiltzius, P. (1997) *Nature*, **385**, 321.

117 Dinsmore, A.D., Yodh, A.G., and Pine, D.J. (1996) *Nature*, **383**, 239.

118 Trau, M., Saville, D.A., and Aksay, I.A. (1996) *Science*, **272**, 706.

119 van Blaaderen, A. and Wiltzius, P. (1995) *Science*, **270**, 1177.

120 Mason, T.G. and Weitz, D.A. (1995) *Phys. Rev. Lett.*, **75**, 2770.

121 Segre, P.N., Behrend, O.P., and Pusey, P.N. (1995b) *Phys. Rev. E*, **52**, 5070.

122 Ilett, S.M., Orrock, A., Poon, W.C.K., and Pusey, P.N. (1995) *Phys. Rev. E*, **51**, 1344.

123 van Megen, W. and Underwood, S.M. (1994) *Phys. Rev. E*, **49**, 4206.

124 van Megen, W. and Underwood, S.M. (1993) *Phys. Rev. Lett.*, **70**, 2766.

125 van Blaaderen, A. and Vrij, A. (1992) *Langmuir*, **8**, 2921.

126 Bartsch, E., Antonietti, M., Schupp, W., and Sillescu, H. (1992) *J. Chem. Phys.*, **97**, 3950.

127 Schatzel, K. and Ackerson, B.J. (1992) *Phys. Rev. Lett.*, **68**, 337.

128 van Megen, W., Underwood, S.M., and Pusey, P.N. (1991) *Phys. Rev. Lett.*, **67**, 1586.

129 van Megen, W. and Pusey, P.N. (1991) *Phys. Rev. A*, **43**, 5429.

130 Pusey, P.N., van Megen, W., Bartlett, P., Ackerson, B.J., Rarity, J.G., and Underwood, S.M. (1989) *Phys. Rev. Lett.*, **63**, 2753.

131 Pusey, P.N. and van Megen, W. (1987) *Phys. Rev. Lett.*, **59**, 2083.

132 Pusey, P.N. (1987) *De Physique*, **48**, 709.

133 Chen, D.T., Lau, A.W.C., Hough, L.A., Islam, M.F., Lubensky, T.C., and Yodh, A.G. (2007) *Phys. Rev. Lett.*, **99**, 148302.

134 Lau, A.W.C., Hoffman, B.D., Davies, A., Crocker, J.C., and Lubensky, T.C. (2003b) *Phys. Rev. Lett.*, **91**, 198101.

135 Levine, A.J. and Lubensky, T.C. (2000) *Phys. Rev. Lett.*, **85**, 1774.

136 Crocker, J.C., Valentine, M.T., Weeks, E.R., Gisler, T., Kaplan, P.D., Yodh, A.G., and Weitz, D.A. (2000) *Phys. Rev. Lett.*, **85**, 888.

137 MacKintosh, F.C. and Schmidt, C.F. (1999) *Curr. Opin. Colloid Interface. Sci.*, **4**, 300.

138 Palmer, A., Mason, T.G., Xu, J.Y., Kuo, S.C., and Wirtz, D. (1999) *Biophysical*, **76**, 1063.

139 Mason, T.G., Ganesan, K., van Zanten, J.H., Wirtz, D., and Kuo, S.C. (1997) *Phys. Rev. Lett.*, **79**, 3282.

140 Gittes, F., Schnurr, B., Olmsted, P.D., MacKintosh, F.C., and Schmidt, C.F. (1997) *Phys. Rev. Lett.*, **79**, 3286.

141 Alsayed, A.M., Islam, M.F., Zhang, J., Collings, P.J., and Yodh, A.G. (2005) *Science*, **309**, 1207.

142 Alsayed, A., Dogic, Z., and Yodh, A. (2004) *Phys. Rev. Lett.*, **93**, 057801.

143 Islam, M.F., Alsayed, A.M., Dogic, Z., Zhang, J., Lubensky, T.C., and Yodh, A.G. (2004) *Phys. Rev. Lett.*, **92**, 088303.

144 Islam, M., Nobili, M., Ye, F., Lubensky, T., and Yodh, A. (2005) *Phys. Rev. Lett.*, **95**, 148301.

145 Pelton, R. (2000) *Adv. Colloid Interface Sci.*, **85**, 1.

146 Senff, H. and Richtering, W.J. (1999) *Chem. Phys.*, **111**, 1705.

147 Stieger, M., Richtering, W., Pedersen, J.S., and Lindner, P. (2004) *J. Chem. Phys.*, **120**, 6197.

148 Shibayama, M. and Tanaka, T. (1993) *Adv. Polym. Sci.*, **109**, 1.

149 Kokufuta, E., Zhang, Y., Tanaka, T., and Mamada, A. (1993) *Macromolecules*, **26**, 1053.

150 Shibayama, M., Tanaka, T., and Han, C. (1992) *J. Chem. Phys.*, **97**, 6829.

151 Shibayama, M., Tanaka, T., and Han, C. (1992) *J. Chem. Phys.*, **97**, 6842.

152 Li, Y. and Tanaka, T. (1992) *Annu. Rev. Mater. Sci.*, **22**, 243.

153 Tokuhiro, T., Amiya, T., Mamada, A., and Tanaka, T. (1991) *Macromolecules*, **24**, 2936.

154 Hirotsu, S., Hirokawa, Y., and Tanaka, T. (1987) *J. Chem. Phys.*, **87**, 1392.

155 Otake, K., Inomata, H., Konno, M., and Saito, S. (1990) *Macromolecules*, **23**, 283.

156 Debord, J.D., Eustis, S., Debord, S.B., Lofye, M.T., and Lyon, L.A. (2002) *Adv. Mater.*, **14**, 658.

157 Wu, J., Huang, G., and Hu, Z. (2003a) *Macromolecules*, **36**, 440.

158 Wu, J., Zhou, B., and Hu, Z. (2003b) *Phys. Rev. Lett.*, **90**, 048304.

159 Han, Y., Ha, N.Y., Alsayed, A.M., and Yodh, A.G. (2008a) *Phys. Rev. E*, **77**, 041406.

160 Han, Y., Yair, S., Alsayed, A.M., Yunker, P., Lubensky, T.C., and Yodh, A.G. (2008b) *Nature*, **456**, 898.

161 Yunker, P., Zhang, Z., Aptowicz, K.B., and Yodh, A.G. (2009) *Phys. Rev. Lett.*, **103**, 115701.

162 Yunker, P., Zhang, Z., and Yodh, A.G. (2010) *Phys. Rev. Lett.*, **104**, 015701.

163 Zhang, Z., Xu, N., Chen, D.T.N., Yunker, P., Alsayed, A.M., Aptowicz, K., Habdas, P., Liu, A.J., Nagel, S., and Yodh, A.G. (2009) *Nature*, **459**, 230. (a) Chen, K., Ellenbroek, W.G., Zhang, Z.X., Chen, D.T.N., Yunker, P.J., Henkes, S., Brito, C., Dauchot, O., van Saarloos, W., Liu, A.J., and Yodh, A.G. (2010) *Phys. Rev. Lett.*, **105**, 025501. (b) Peng, Y., Wang, Z., Alsayed, A.M., Yodh, A.G., and Han, Y. (2010) *Phys. Rev. Lett.*, **20**, 205703. (c) Wang, Z,-R., Alsayed A.M., Yodh, A.G. and Han, Y. (2010) *J. Chem. Phys.*, **132**, 154501.

164 Berne, B.J. and Pecora, R. (2000) *Dynamic Light Scattering: With Applications to Chemistry, Biology, and Physics*, Dover Publications, Inc., Mineola, NY.

165 Johnson, C.S. and Gabriel, D.A. (1994) *Laser Light Scattering*, Dover Publications, Inc., Mineola, NY.

166 Pronk, S. and Frenkel, D. (2004) *Phys. Rev. E*, **69**, 066123.

167 Baumgartl, J. and Bechinger, C. (2005) *Europhys. Lett.*, **71**, 487.

168 Polin, M., Grier, D.G., and Han, Y. (2007) *Phys. Rev. E*, **76**, 041406.

169 Behrens, S.H. and Grier, D.G. (2001) *Phys. Rev. E*, **64**, 050401.

170 Han, Y. and Grier, D.G. (2003) *Phys. Rev. Lett.*, **91**, 038302.

171 Chan, E.M. (1977) *J. Phys. C*, **10**, 3477.

172 Hansen, J.P. and McDonald, I.R. (1986) *Theory of Simple Liquids*, 2nd edn, Academic, New York.

173 Stieger, M., Pedersen, J.S., Lindner, P., and Richtering, W. (2004) *Langmuir*, **20**, 7283.

174 Dash, J.G. (1999) *Rev. Mod. Phy.*, **71**, 1737.

175 Löwen, H. (1994) *Phys. Rep.*, **237**, 249.

176 Dash, J.G., Fu, H., and Wettlaufer, J.S. (1995) *Rep. Prog. Phys.*, **58**, 115.

177 Cahn, R.W. (2001) *Nature*, **413**, 582.

178 Lindemann, F.A. (1910) *Z. Phys.*, **11**, 609.

179 Edwards, S.F. and Warner, M. (1979) *Philos. Mag.*, **40**, 257.

180 Burakovsky, L., Preston, D.L., and Silbar, R.R. (2000) *Phys. Rev. B*, **61**, 15011.

181 Lipowsky, R. (1986) *Phys. Rev. Lett.*, **57**, 2876.

182 Ciccotti, G., Guillope, M., and Pontikis, V. (1983) *Phys. Rev. B*, **27**, 5576.

183 Curtin, W.A. (1989) *Phys. Rev. B*, **39**, 6775.

184 Pluis, B., Frenkel, D., and van der Veen, J.F. (1990) *Surf. Sci.*, **239**, 282.

185 Ohnesorge, R., Löwen, H., and Wagner, H. (1994) *Phys. Rev. E*, **50**, 4801.

186 Lipowsky, R., Breuer, U., Prince, K.C., and Bonzel, H.P. (1989) *Phys. Rev. Lett.*, **62**, 913.

187 Cahn, R.W. (1989) *Nature*, **323**, 668.

188 Pettersen, M.S., Lysek, M.J., and Goodstein, D.L. (1989) *Phys. Rev. B*, **40**, 4938.

189 Dahmen, U., Hagege, S., Faudot, F., Radetic, T., and Johnson, E. (2004) *Philos. Mag.*, **84**, 2651.

190 Frenken, J.W.M. and van der Veen, J.F. (1985) *Phys. Rev. Lett.*, **54**, 134.

191 van der Veen, J.F. (1999) *Surf. Sci.*, **433–435**, 1.

192 Pluis, B., van der Gon, A.W.D., Frenken, J.W.M., and van der Veen, J.F. (1987) *Phys. Rev. Lett.*, **59**, 2678.

193 Broughton, J.Q. and Gilmer, G. (1986) *Phys. Rev. Lett.*, **56**, 2692.

194 Phillpot, S., Lutsko, J.F., Wolf, D., and Yip, S. (1989) *Phys. Rev. B*, **40**, 2831.

195 Kikuchi, R. and Cahn, J. (1980) *Phys. Rev. B*, **21**, 1893.

196 Nguyen, T. and Yip, S. (1989) *Mater. Sci. Eng. A: Struct.*, **107**, 15.

197 Ho, P.S., Kwok, T., Nguyen, T., Nitta, C., and Yip, S. (1985) *Scripta. Math.*, **19**, 993.

198 Hsieh, T.E. and Balluffi, R.W. (1989) *Acta Meter.*, **37**, 1637.

199 Zhu, J., Li, M., Rogers, R., Meyer, W., Ottewill, R.H., Crew, S.-S.S., Russel, W.B., and Chaikin, P.M. (1997b) *Nature*, **387**, 883.

200 Hirth, J.P. and Lothe, J. (1982) *Theory of Dislocations*, 2nd edn, John Wiley & Sons, Inc., New York.

201 Alsayed, A.M., Han, Y., Aptowicz, K., and Yodh, A.G., *Phys. Rev. E*, in press.

202 Bongers, J. and Versmold, H. (1996) *J. Chem. Phys.*, **104**, 1519.

203 Ohshima, Y.N. and Nishio, I. (2001) *J. Chem. Phys.*, **114**, 8649.

204 Schall, P., Cohen, I., Weitz, D.A., and Spaepen, F. (2004) *Science*, **305**, 1944.

205 Pronk, S. and Frenkel, D. (1999) *J. Chem. Phys.*, **110**, 4589.

206 Strandburg, K. (1992) *Bond-Orientational Order in Condensed Matter Systems*, Springer, New York.

207 Nelson, D.R. (2002) *Defects and Geometry in Condensed Matter Physics*, Cambridge University Press, Cambridge.

208 Peierls, R.E. (1934) *Helv. Phys. Acta*, **7**, 81.

209 Landau, L.D. and Lifshitz, E.M. (1980) *Statistical Physics*, Part I, Pergamon, Oxford.

210 Landau, L.D. (1937) *Phys. Z. Sowjetunion*, **11**, 26.

211 Mermin, N.D. and Wagner, H. (1966) *Phys. Rev. Lett.*, **17**, 1133.

212 Mermin, N.D. (1968) *Phys. Rev.*, **176**, 250.

213 Kosterlitz, J.M. and Thouless, D.J. (1973) *J. Phys. C: Solid State Physics*, **6**, 1181.

214 Nelson, D.R. and Halperin, B.I. (1979) *Phys. Rev. B*, **19**, 2457.

215 Young, A.P. (1979) *Phys. Rev. B*, **19**, 1855.

216 Li, D. and Rice, S.A. (2005) *Phys. Rev. E*, **72**, 041506.

217 Pang, H., Pan, Q., and Song, P.H. (2007) *Phys. Rev. B*, **76**, 064109.

218 Chekmarev, D.S., Oxtoby, D.W., and Rice, S.A. (2001) *Phys. Rev. E*, **63**, 051502.

219 Weber, H., Marx, D., and Binder, K. (1995) *Phys. Rev. B*, **51**, 14636.

220 Zangi, R. and Rice, S.A. (1998) *Phys. Rev. E*, **58**, 7529.

221 Strandburg, K.J. (1988) *Rev. Mod. Phys.*, **60**, 161.

222 Chou, C.F., Jin, A.j., Hui, S.W., Huang, C.C., and Ho, J.T. (1998) *Science*, **280**, 1424.

223 Grier, D.G., Murray, C.A., Bolle, C.A., Gammel, P.L., Bishop, D.J., Mitzi, D.B., and Kapitulnik, A. (1991) *Phys. Rev. Lett.*, **66**, 2270.

224 Angelescu, D.E., Harrison, C.K., Trawick, M.L., Register, R.A., and Chaikin, P.M. (2005) *Phys. Rev. Lett.*, **95**, 025702.

225 Murray, C.A. and Winkle, D.H.V. (1987) *Phys. Rev. Lett.*, **58**, 1200.

226 Marcus, A.H. and Rice, S.A. (1996) *Phys. Rev. Lett.*, **77**, 2577.

227 Karnchanaphanurach, P., Lin, B.H., and Rice, S.A. (2000) *Phys. Rev. E*, **61**, 4036.

228 Zahn, K., Lenke, R., and Maret, G. (1999) *Phys. Rev. Lett.*, **82**, 2721.

229 Zahn, K. and Maret, G. (2000) *Phys. Rev. Lett.*, **85**, 3656.

230 von Grünberg, H.H., Keim, P., Zahn, K., and Maret, G. (2003) *Phys. Rev. Lett.*, **93**, 255703.

231 von Grünberg, H.H., Keim, P., and Maret, G. (2007) *Soft Matter*, **3**, 41.

232 Murray, C.A. and Grier, D.G. (1996) *Annu. Rev. Phys. Chem.*, **47**, 421.

233 van Winkle, D.H. and Murray, C.A. (1986) *Phys. Rev. A*, **34**, 562.

234 Lin, S.Z., Zheng, B., and Trimper, S. (2006) *Phys. Rev. E*, **73**, 066106.

235 Zollweg, J.A. and Chester, G.V. (1992) *Phys. Rev. B*, **46**, 11186.

236 Fernandez, J.F., Alonso, J.J., and Stankiewicz, J. (1995) *Phys. Rev. Lett.*, **75**, 3477.

237 Jaster, A. (1998) *Europhys. Lett.*, **42**, 277.

238 Jaster, A. (2004) *Phys. Lett. A*, **330**, 120. (a) Mak, C.H. (2006) *Phys. Rev. E*, **73**, 065104.

239 Celestini, F., Ercolessi, F., and Tosatti, E. (1997) *Phys. Rev. Lett.*, **78**, 3153. (a) Bedanov, V.M., Gadiyak, G.V., and Lozovik, Y.E. (1985) *Phys. Lett. A*, **109**, 289.

240 von Grünberg, H.H., Keim, P., Zahn, K., and Maret, G. (2004) *Phys. Rev. Lett.*, **93**, 255703.

241 Keim, P., Maret, G., and von Grünberg, H.H. (2007) *Phys. Rev. E*, **75**, 031402.

242 Ubbelohde, A.R. (1965) *Melting and Crystal Structure*, Clarendon, Oxford.

243 Binder, K. (1987) *Rep. Prog. Phys.*, **50**, 783.

244 Wannier, G.H. (1950) *Phys. Rev.*, **79**, 357.

245 Wannier, G.H. (1973) *Phys. Rev. B: Erratum*, **7**, 5017.

246 Blote, H.W.J. and Nienhuis, B. (1994) *Phys. Rev. Lett.*, **72**, 1372.

247 Moessner, R. and Ramirez, A.R. (2006) *Phys. Today*, **59**, 24.

248 Pauling, L. (1935) *J. Am. Chem. Soc.*, **57**, 2680.

249 Harris, M.J., Bramwell, S.T., McMorrow, D.F., Zeiske, T., and Godfrey, K.W. (1997) *Phys. Rev. Lett.*, **79**, 2554.

250 Nakatsuji, S., Nambu, Y., Tonomura, H., Sakai, O., Jonas, S., Broholm, C., Tsunetsugu, H., Qiu, Y., and Maeno, Y. (2005) *Science*, **309**, 1697.

251 Bramwell, S.T. and Gingras, M.J.P. (2001) *Science*, **294**, 1495.

252 Moessner, R. (2001) *Can. J. Phys.*, **79**, 1283.

253 Ramirez, A.R. (2003) *Nature*, **421**, 483.

254 Anderson, P.W. (1987) *Science*, **235**, 1196.

255 Davidovic, D., Kumar, S., Reich, D.H., Siegel, J., Field, S.B., Tiberio, R.C., Hey, R., and Ploog, K. (1996) *Phys. Rev. Lett.*, **76**, 815.

256 Davidovic, D., Kumar, S., Reich, D.H., Siegel, J., Field, S.B., Tiberio, R.C., Hey, R., and Ploog, K. (1997) *Phys. Rev. B*, **55**, 6518.

257 Hilgenkamp, H., Ariando, A., Smilde, H.H., Blank, D.H.A., Rijnders, G., Rogalla, H., Kirtley, J.R., and Tsueiet, C.C. (2003) *Nature*, **422**, 50.

258 Kirtley, J.R., Tsuei, C.C., Ariando, A., Smilde, J.J.H., and Hilgenkamp, H. (2005) *Phys. Rev. B* **72** 214521.

259 Wang R.W. *et al.* (2006) *Nature*, **439**, 303.

260 Libal, A., Reichhardt, C., and Reichhardt, C.J.O. (2006) *Phys. Rev. Lett.*, **97**, 228302.

261 Koshikiya, Y. and Hachisu, S. (1982) Proceedings of the Colloid Symposium of Japan (in Japanese, 1982).

262 Pieranski, P., Strzlecki, L., and Pansu, B. (1983) *Phys. Rev. Lett.*, **50**, 900.

263 Ogawa, T. (1983) *J. Phys. Soc. Jpn.* (Suppl.), **52**, 167.

264 Chou, T. and Nelson, D.R. (1993) *Phys. Rev. E*, **48**, 4611.

265 Weiss, J.A., Oxtoby, D.W., Grier, D., and Murray, C.A. (1995) *J. Chem. Phys.*, **103**, 1180.

266 Schmidt, M. and Lowen, H. (1996) *Phys. Rev. Lett.*, **76**, 4552.

267 Schmidt, M. and Lowen, H. (1997) *Phys. Rev. E*, **55**, 7228.

268 Houtappel, R.M.F. (1950) *Physica*, **16**, 425.

269 Melko, R.G., den Hertog, B.C., and Gingras, M.J.P. (2001) *Phys. Rev. Lett.*, **87**, 067203.

270 Millane, R.P. and Blakeley, N.D. (2004) *Phys. Rev. E*, **70**, 057101.

271 Chen, Z.Y. and Kardar, M. (1986) *J. Phys. C: Solid State Physics*, **19**, 6825.

272 Gu, L., Chakraborty, B., Garrido, P.L., Phani, M., and Lebowitz, J.L. (1996) *Phys. Rev. B*, **53**, 11985.

273 Osterman, N., Babic, D., Poberaj, I., Dobnikar, J., and Ziherl, P. (2007) *Phys. Rev. Lett.*, **99**, 248301.

274 Mau, S.C. and Huse, D.A. (1999) *Phys. Rev. E*, **59**, 4396.

275 Phillips, J. (1996) *Rep. Prog. Phys.*, **59**, 1133.

276 Lohr, M.A., Alsayed, A.M., Chen, B.G., Zhang, Z., Kamien, R.D., and Yodh, A.G. (2010) *Phys. Rev. E*, **81**, 040401.